Cohesin mediated loop extrusion from active enhancers form chromatin jets in *C. elegans*

Jun Kim[1], Haoyu Wang[1], Sevinç Ercan[1#]

[1] Department of Biology, Center for Genomics and Systems Biology, New York University, New York, NY, USA

[#] corresponding author
email: sevinc@nyu.edu

Abstract

In mammals, cohesin and CTCF organize the 3D genome into topologically associated domains (TADs) to regulate communication between cis-regulatory elements. However, many organisms, including *S. cerevisiae*, *C. elegans*, and *A. thaliana* lack CTCF. Here, we use *C. elegans* as a model to investigate the function of cohesin in 3D genome organization in an animal without CTCF. We use auxin-inducible degradation to acutely deplete SMC-3 or its negative regulator WAPL-1 from somatic cells. Using Hi-C data, we identify a cohesin-dependent 3D genome organization feature called chromatin jets (aka fountains). These are population average reflections of DNA loops that are ~20-40 kb in scale and often cover a few transcribed genes. The jets emerge from NIPBL occupied segments, and the trajectory of the jets coincides with cohesin binding. Cohesin translocation from jet origins depends on a fully intact complex and is extended upon WAPL-1 depletion. Hi-C results support the idea that cohesin is preferentially loaded at NIPBL occupied sites and loop extrudes in an effectively two-sided manner. The location of putative loading sites coincide with active enhancers and the strength of chromatin jet pattern correlates with transcription. Hi-C analyses upon WAPL-1 depletion reveal unequal loop extrusion processivity on each side and stalling due to cohesin molecules colliding. Compared to mammalian systems, average processivity of *C. elegans* cohesin is ~10-fold shorter and NIPBL binding does not depend on cohesin. We conclude that the processivity of cohesin scales with genome size; and regardless of CTCF presence, preferential loading of cohesin at enhancers is a conserved mechanism of genome organization that regulates the interaction of gene regulatory elements in 3D.

Introduction

In mammalian genomes, cohesin and CTCF form topologically associating domains (TADs) (da Costa-Nunes and Noordermeer 2023). The earlier models of TAD formation encompassed three main features, cohesin is uniformly loaded, cohesin performs two-sided loop extrusion, and loop extrusion is stalled at CTCF-binding sites located at TAD boundaries (Fudenberg et al. 2017).

The second and the third assumptions of the model were visualized *in vitro* using single-molecule assays, thus bridging the gap between the theoretical model and the experimental observation *in vivo* (Kim et al. 2019; Davidson et al. 2023). Further studies refined the earlier models and proposed mechanistic variations of two-sided loop extrusion (e.g. frequent switching of direction in a one-sided extrusion scheme), effect of cohesin molecules meeting one another (resulting in bypassing to form secondary folds in loops or colliding and stopping extrusion on one side), and specific proteins controlling loop extrusion as loader/facilitator (NIPBL), remover (WAPL), or acting as barriers (e.g. MCM complex, RNA Pol II, DNA topology) (Dequeker et al. 2022; Morao et al. 2022; Banigan et al. 2023; Corsi et al. 2023).

Recent studies also required an update to uniform loading assumption, as cohesin may be preferentially loaded at specific sites, leading to the formation of Hi-C detected features termed "jets", "plumes" or "fountains" depicted as secondary diagonals protruding from narrow segments (Wike et al. 2021; Guo et al. 2022). The preferential loading sites locally increase the frequency of cohesin-mediated loops, thus providing another layer of 3D genome folding, which is shorter in scale compared to TADs. Such a mechanism of genome folding could have strong regulatory implications for species lacking CTCF.

Caenorhabditis elegans is a small animal with ~100 Mb genome and no CTCF (Heger et al. 2009). A total of approximately ~20,000 genes are closely located to each other. Median gene length is ~2 kb and intergenic distances between genes (excluding operons encompassing ~15% of genes) range from ~2 to 10 kb (Nelson et al. 2004; Girard et al. 2007; Allen et al. 2011). Like other species, enhancers are distinguished from promoters based on enrichment of distinct and conserved histone modifications, including H3K27 acetylation and H3K4 methylation (Evans et al. 2016; Daugherty et al. 2017). Mapping enhancer chromatin features and analyses of several individual genes suggest that most enhancers are located ~ 2kb from promoters but some enhancers can be up to ~12 kb away (Shi et al. 2009).

In the mammalian system, somatic cohesin is composed of four subunits, SMC1, SMC3, RAD21, and STAG (Hassler et al. 2018). The STAG subunit has two isoforms STAG1 and STAG2 that forms cohesin in mutually exclusive manner (Cuadrado and Losada 2020). Several subunits of mammalian cohesin are specific for meiosis (Ishiguro 2019). In *C. elegans*, the three of the four subunits of cohesin, SMC-1, SMC-3, and SCC-3 (STAG), has a single copy, while the kleisin subunit has 5 variants: COH-1, COH-2 (aka SCC-1), COH-3, COH-4, and REC-8 (Severson et al. 2009; Wood et al. 2010). COH-2, but not COH-1, has mitotic functions, while COH-3/4 (paralogs) and REC-8 have meiotic functions (Mito et al. 2003; Severson and Meyer 2014; Hernandez et al. 2018; Yu et al. 2023). We reasoned that analyses of cohesin binding and 3D genome organization upon rapid depletion of SMC-3 and its negative regulator WAPL-1 would reveal cohesin function in *C. elegans* genome organization.

To do this, we applied auxin-inducible degradation to SMC-3 or its negative regulator WAPL-1 from somatic cells in *C. elegans* early-L3 larvae with 1 hour auxin treatment. We performed Hi-C analyses in control, SMC-3 and WAPL-1 depletion conditions, and identified over 250 cohesin-dependent chromatin jets. Upon depletion of SMC-3 or WAPL-1, the jets are lost or extended, respectively. The jets emerge from the cohesin loader NIPBL occupied segments that frequently overlap with active enhancers, and the trajectory of the jets coincides with cohesin

binding. Processivity of bi-directional cohesin loop extrusion is unequal on each side and may reflect the combinatory effects of transcription and clashes between incoming and outgoing cohesin molecules. Hi-C analysis of 3D DNA contacts in the control, SMC-3 and WAPL depleted conditions suggest that the average size of the cohesin mediated DNA loops in *C. elegan*s is ~15 kb. One hour depletion of SMC-3 or WAPL-1 does not affect the binding of RNA Polymerase II and NIPBL. Together, our results suggest that cohesin is preferentially loaded at NIPBL occupied active enhancers, from which cohesin loop extrudes bi-directionally. These transient yet highly frequent cohesin loops appear as "jets" on Hi-C maps and are a conserved 3D genome organization feature that is sub-TAD in scale and occurs regardless of CTCF presence.

Materials and Methods

Worm strain and growth

Worms were grown and maintained at 20-22°C on Nematode Growth Medium (NGM) plates containing *E. coli* strains OP50-1 and/or HB101. To isolate synchronized L2/L3 worms, gravid adults were bleached in 0.5 M NaOH and 1.2% bleach, and embryos were hatched overnight in M9 buffer (22 mM KH2PO4 monobasic, 42.3 mM Na2HPO4, 85.6 mM NaCl, 1mM MgSO4). The resulting starved L1s were grown for 24 hours at 22°C. Degron-GFP tagged alleles were produced by SUNY Biotech and crossed to CA1200 strain expressing TIR1 under the control of eft-3 promoter to produce ERC102 syb5520 [smc-3::GGGGS::AID::emGFP] III , [eft-3p::TIR1::mRuby::unc-54 3'UTR + Cbr-unc-119(+)] II and ERC103 syb6035 [wapl-1::GGGGS::AID::emGFP] IV, [eft-3p::TIR1::mRuby::unc-54 3'UTR + Cbr-unc-119(+)] II.

Auxin treatment

Auxin (indole-3-acetic-acid, Fisher 87-51-4) was resuspended in 100% ethanol to a concentration of 400 mM. Plates were prepared by adding resuspended auxin at a concentration of 1 mMto NGM media before pouring. Synchronized L2/L3 worms were washed three times with M9 and split into two. Half of the worms were transferred to NGM 10 cm plates containing 1mM of auxin. The other half were placed in normal NGM 10 cm plates (no-auxin control). A maximum of 300µL of settled worms was placed in one 10 cm plate. Worms were then washed one time with M9 and processed according to future application. For ChIP and Hi-C, worms were crosslinked in 2% formaldehyde for 30 minutes, followed by quenching in 125mM glycine for 5 minutes, one wash with M9 and two washes with PBS, PMSF and protease inhibitors. For RNA-seq, worms were stored in Trizol.

Microscopy

The worms were washed off the plate in M9 buffer, crosslinked in 0.5% formaldehyde for 15 minutes and 'freeze cracked' by submerging in liquid nitrogen for 1 minute and then thawing in a 37°C water bath. The worms were washed twice using 70% ethanol followed by a third wash using the wash buffer (PBS-0.05% Tween-20). The worms were resuspended in 1mL of wash buffer and 1ul of 2ug/mL DAPI (FisherEN62248) and were incubated in 37°C water bath for 30 minutes. The worms were then washed twice in PBS and imaged on slides for DAPI and GFP.

ChIP-seq

Two biological replicates with matching input samples were performed for each experiment. Around 100 µL of L2/L3 larvae were dounce-homogenized with 30 strokes in FA buffer (50 mM HEPES/KOH pH 7.5, 1 mM EDTA, 1% Triton X-100, 0.1% sodium deoxycholate, 150 mM NaCl) supplemented with PMSF and protease inhibitors (Calbiochem, 539131). Dounced worms were sonicated in 0.1% sarkosyl for 15 minutes using a Picoruptor to obtain chromatin fragments between 200 and 800 bp. Protein concentration was determined using Bradford assay (Biorad 500-0006). 1-2 mg of protein extract was used per ChIP and 5% was taken out to use as input DNA. The remaining protein extract was incubated with 3 to 10 ug of antibody at 4°C rotating overnight in a volume of 440µL. 40µL of (1:1V) Protein A and/or G Sepharose beads that were previously washed 3 times with FA buffer, were added and incubated, rotating at 4°C for 2 hours. Beads were washed with 1mL of each of the following buffers: 2 times with FA buffer, 1 time with FA-1mM NaCl buffer, 1 time with FA-500mM NaCl buffer, 1 time with TEL buffer (0.25 M LiCl, 1% NP-40, 1% sodium deoxycholate, 1 mM EDTA, 10 mM Tris-HCl, pH 8.0) and 2 times with TE buffer. Immunoprecipitated chromatin was eluted from beads by incubating in ChIP elution buffer (1% SDS, 250 mM NaCl, 10 mM Tris pH 8.0, 1 mM EDTA) at 65°C for 30 minutes, treated with Proteinase K and reverse crosslinked at 65°C overnight. Half of the ChIP DNA and 30 ng of input DNA were used for library preparation. End repair was performed in T4 ligase reaction buffer (New England Biolabs, NEB), 0.4mM of dNTPs, 20 U of T4 Polynucleotide kinase (NEB), 3.5 U of Large (Klenow) fragment (NEB) and 6 U of T4 DNA polymerase for 30 minutes at 20°C in a total volume of 33 µL. Reaction was cleaned using Qiagen MinElute PCR purification kit. A-tailing reaction was performed in NEB buffer 2, 0.2 mM of dATPs and 7.5 U of Klenow fragment-exo (NEB) at 37°C for 60 minutes in 25 µL. Reaction was cleaned using Qiagen MinElute PCR purification kit. Illumina TruSeq adapters were ligated to DNA fragments in a reaction containing 2X Quick ligation buffer (NEB), 0.25 µM of adapter and 2 µL of Quick ligase (NEB) for 20 minutes at 23°C in 40 µL. Reaction was cleaned using Agencourt AMPure XP beads and the eluted DNA was PCR amplified in 50 µL using Phusion Polymerase and TruSeq primers, forward: AAT GAT ACG GCG ACC ACC GAG ATC TAC ACT CTT TCC CTA CAC G*A, reverse: CAA GCA GAA GAC GGC ATA CGA GA*T, where * represents a phosphorothioate bond. PCR reactions were cleaned using Qiagen MinElute PCR purification kit. The eluted DNA was run on a 1.5% agarose gel and fragments between 250-600 bp were gel extracted using Qiagen gel extraction kit. Library concentration was determined using KAPA Library quantification kit. Single-end 75 bp sequencing was performed using the Illumina NextSeq 500.

ChIP-seq data analysis: Bowtie2 version 2.4.2 was used to align 75 bp single-end reads to WS220 with default parameters (Langmead and Salzberg 2012). Bam sorting and indexing was performed using samtools version 1.11 (Danecek et al. 2021). BamCompare tool in Deeptools version 3.5.0 was used to normalize for the sequencing depth using CPM and create ChIP-Input coverage with a bin size of 10 bp and 200 bp read extension (Ramirez-Gonzalez et al. 2012). Only reads with a minimum mapping quality of 20 were used, and mitochondrial DNA, PCR duplicates, and blacklisted regions were removed (Amemiya et al. 2019). The average coverage data was generated by averaging ChIP-Input enrichment scores per 10 bp bins across the genome. ChIP-seq peaks are identified using MACS2 version 2.1.1 (https://github.com/macs3-project/MACS). Peaks are called using both the individual replicates and combined bam files with minimum false discovery rate of 0.05. The peaks shown below average ChIP-seq tracks are peaks called using the combined bam files, whereas the peaks shown below individual replicates

are peaks called using the corresponding replicate.

Hi-C

Two biological replicates were performed for each experiment. Crosslinked L2/L3 worms collected as described above were resuspended in 20 ul of PBS per 50ul of worm pellet, then dripped into liquid nitrogen containing mortar. The worms were grounded with pestle until fine powder. Grounded worms were crosslinked again in 2% formaldehyde using the TC buffer as described by the Arima High Coverage Hi-C kit, which uses four 4-base cutters, DpnII, HinfI, DdeI, and MseI. The Arima manufacturer's protocol was followed including the recommended method of the library preparation using KAPA Hyper Prep Kit. Paired-end 100 bp sequencing was performed using the Illumina Novaseq 6000.

Hi-C data analysis: The Hi-C data was mapped to ce10 (WS220) reference genome using default parameters of the Juicer pipeline version 1.5.7 (Durand et al. 2016). The biological replicates were combined using juicer's mega.sh script. The mapping statistics from the inter_30.txt output file are provided. The inter_30.hic outputs were converted to cool format using the hicConvertFormat of HiCExplorer version 3.6 (Ramirez et al. 2018; Wolff et al. 2018) in two steps using the following parameters: 1) --inputFormat hic, --outputFormat cool, 2) --inputFormat cool --outputFormat cool --load_raw_values. The cool file was balanced using cooler version 0.8.11 using the parameters: --max-iters 500, --mad-max 5, --ignore-diags 2 (Abdennur and Mirny 2020). The balanced cool file was used for all downstream analysis.
For computing log-binned P(s) and its log-derivative cooltools version 0.4.0 (https://github.com/open2c/cooltools) was used. For visualizing ChIP-seq data with Hi-C data in python, pyBigwig version 0.3.18 (https://github.com/deeptools/pyBigWig) was used.

Fontanka (Galitsyna et al. 2023) was used with the following steps. (i) Snippets extraction: we manually identified three different types of shapes based on the tilt of the jet: center, left, and right. We manually inspected each snippet of the jets that were identified based on the insulation score as described in the Supplemental Figure 2. We manually selected 10 snippets that appeared to show left or right tilt. For each shape, the 10 snippets were used to generate observed-over-expected on-diagonal pile-up matrices with flanking +/-100kb window. This pile-up is used as the 'reference mask' to which the snippets from the rest of the genome is compared to. (ii) Fountain score and Scharr score: we used the fontanka slice-windows function to generate genome-wide snippets using the parameter -W 100_000 for both control condition and WAPL depletion conditions using 2 kb binned matrix. Fountain and Scharr score for each window was calculated by Fontanka-apply-fountain-mask. (iii) Peak calling and Thresholding: we applied otsu thresholding method on peak prominence returned from fontanka-apply-fountain-mask function and applied a minimum threshold of 0.2 for fountain score. Scharr score, which measures the uniformity/sharpness of the Hi-C matrix, can be used to infer rearrangements and incomplete reference genome data. Windows of Hi-C matrix with sharp transitions, which often arises from imperfect reference genome (rearrangements and missing segments), have higher Scharr score, whereas windows containing smooth transitions in contact scores have lower Scharr score. We only removed the top scoring 5% of candidate fountains (false positives due to reference genome) based on previous work showing that long-read assembly of *C. elegans* genome only added 1.8 Mb (<2%) to the existing reference genome (Yoshimura et al. 2019). (iv) Leveraging WAPL condition: we kept control fountains that overlapped (+/- 10 kb) with those

called in the WAPL depletion which shows sharper contrast in fountain shapes. (vi) Validation: we ensured that the average on-diagonal pile-up of the called fountains shows distinct shapes.

mRNA-seq
L3 larvae were collected and stored in Trizol (Invitrogen) at -70°C. Total RNA was extracted through the freeze-crack method and processed as described previously (Albritton et al. 2014). RNA was cleaned up using Qiagen RNeasy MinElute Cleanup kit. mRNAs were purified using Sera-Mag Oligo (dT) beads (Thermo Scientific), then fragmented using Ambion (AM8740), and cleaned using Qiagen RNAeasy minElute kit. RNA was reverse transcribed using Superscript III system (Invitrogen, 18080-051). Residual dNTP was removed using ethanol precipitation. The second strand was synthesized using DNA polymerase I (Invitrogen). dsDNA was purified using Qiagen DNA minElute kit. Single-stranded illumine libraries were prepared as indicated for ChIP-seq with the following modification: prior to PCR amplification, uridine was digested using Uracil-N-Glycosylase (ThermoScientific EN0361).

mRNA-seq data analysis: Single-end 75 bp sequencing was performed using the Illumina NextSeq 500. Reads were mapped to WS220 (ce10) *C. elegans* genome using HISAT2 version 2.2.1 (Kim et al. 2015) with the parameter --rna-strandness R. The SAM output from HISAT2 and WS220 gtf file were used to calculate counts per gene using HTSeq version 0.13.5 (Anders et al. 2015). The raw counts were normalized FPKM using cufflinks version 2.2.1 (Roberts et al. 2011), and then FPKM was converted to TPM. For comparing between conditions, the raw counts were used for the R package DESeq2 version 1.30.0 (Love et al. 2014).

Sequencing data and analysis script availability
The data are available at the Gene Expression Omnibus under GSE237663. A list of data and statistics are provided in Supplemental File 1. Analysis scripts are provided at https://github.com/ercanlab/2023_Kim_cohesin.

Results

Chromatin jet (aka fountains) is a feature of 3D genome organization detected by Hi-C

C. elegans genome is organized into roughly similar sized chromosomes, including five autosomes and one X chromosome. The chromosomes are holocentric and are partitioned by gene-rich central domains that make inter-chromosomal contacts, and gene-poor left and right arms that are frequently located close to the nuclear lamina (Liu et al. 2011; Ho et al. 2014). Unlike mammalian systems where TADs are observed on all chromosomes, in *C. elegans*, autosomes do not display stereotypical loop-anchored TADs with defined boundaries (Crane et al. 2015; Bian et al. 2020; Sawh and Mango 2022). Instead, loop-anchored TADs are formed on the X chromosomes by an X-specific condensin complex (Anderson et al. 2019; Kim et al. 2022; Morao et al. 2022). Like the mammalian cohesin complex, condensin mediated TADs on the *C. elegans* X chromosomes are mega base pairs (Mb) in scale. We observed that on both the autosomes and X chromosome, smaller than TAD-scale contact domains appear as “jets” on Hi-C maps (Figure 1). Next, we sought to determine if jets are cohesin dependent.

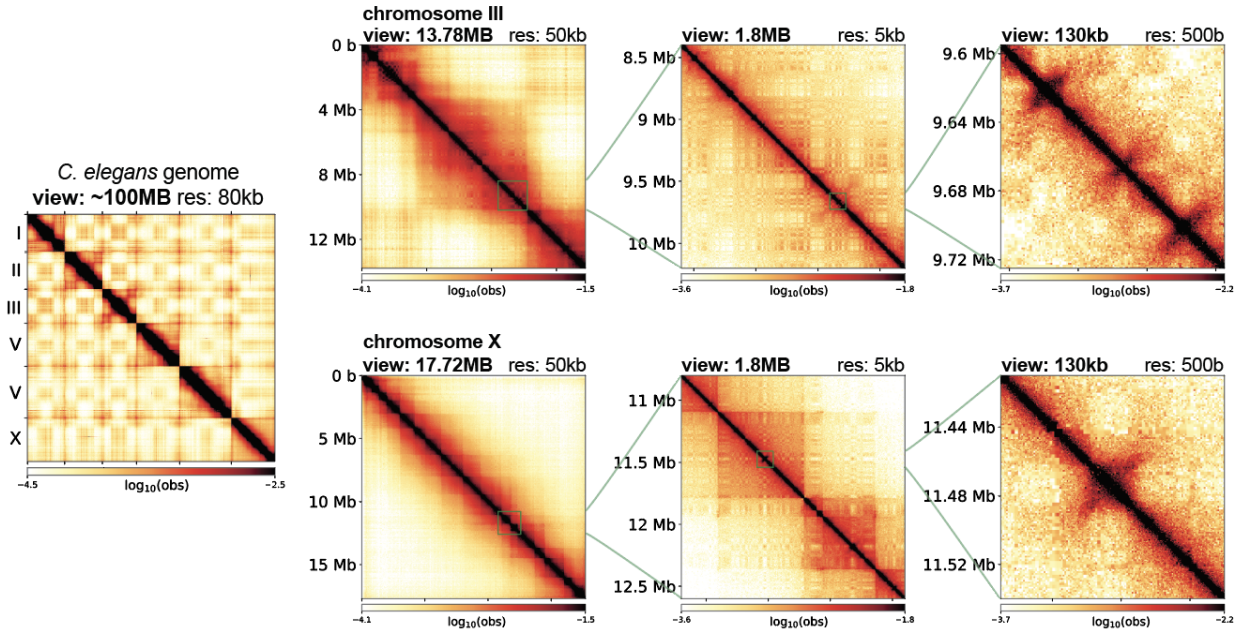

Figure 1. 3D organization of the *C. elegans* genome at different scales.
Leftmost panel shows the Hi-C contact matrix of the entire genome. On the right, chromosome III and the X chromosome, and representative regions are shown at different scales. Rightmost panels highlight chromatin jets that appear as protruding 3D DNA contacts from the main diagonal.

Acute depletion of cohesin and WAPL from somatic cells

In *C. elegans*, there is a singular subunit for SMC-1, SMC-3, and SCC-3 (Figure 2A). To study the effect of cohesin loss, we targeted SMC-3 subunit for auxin inducible degradation. In conjunction, to study the enhanced activity of cohesin, we targeted WAPL (encoded by gene named *wapl-1* in *C. elegans*), a negative regulator of cohesin (Gandhi et al. 2006; Kueng et al. 2006). The *C. elegans* ortholog of the cohesin loader NIPBL is encoded by the gene *pqn-85*/*scc-2* (Lightfoot et al. 2011). The two proteins, SMC-3 and WAPL were C-terminally tagged with degron-gfp at the endogenous locus using strategies employed previously (Zhang et al. 2015; Morao et al. 2022). To analyze somatic cells, we used worms in the early L3 stage, at which point most somatic cells have stopped dividing and the germline has not started proliferating (Sulston and Horvitz 1977). To knock down cohesin specifically in the somatic cells, we used the background strain in which the auxin response gene TIR1 is under the control of a soma-specific promoter *eft-3* (Zhang et al. 2015). This background strain is used as a control where TIR1 is expressed but none of the endogenous genes are tagged with degron-gfp (Figure 2B).

Upon visualizing DAPI and GFP, we observe that in the control condition, both cohesin and WAPL show ubiquitous GFP signals, suggesting that cohesin and WAPL are present in the all interphase as well as the few germ cells present in early L3 larvae (Figure 2C, no auxin). Upon auxin treatment, both cohesin and WAPL are noticeably depleted in somatic cells but are maintained in the germline as expected from somatic expression of TIR1 (Figure 2C, 1hr auxin). At population average, western blot analysis of degron-GFP tagged proteins show noticeable

depletion in the total amount of protein (Figure 2D). This depletion is maximally achieved by 1-hour treatment, and no further depletion was observed upon 2-hour treatment. Therefore, we chose 1-hour as a general 'depletion condition' to minimize the potential indirect effect. Lastly, we performed ChIP-seq using anti-GFP antibodies and observed uniform depletion across the genome (Figure 2E). In summary, both SMC-3 and WAPL are acutely depleted from somatic cells with 1-hour auxin treatment.

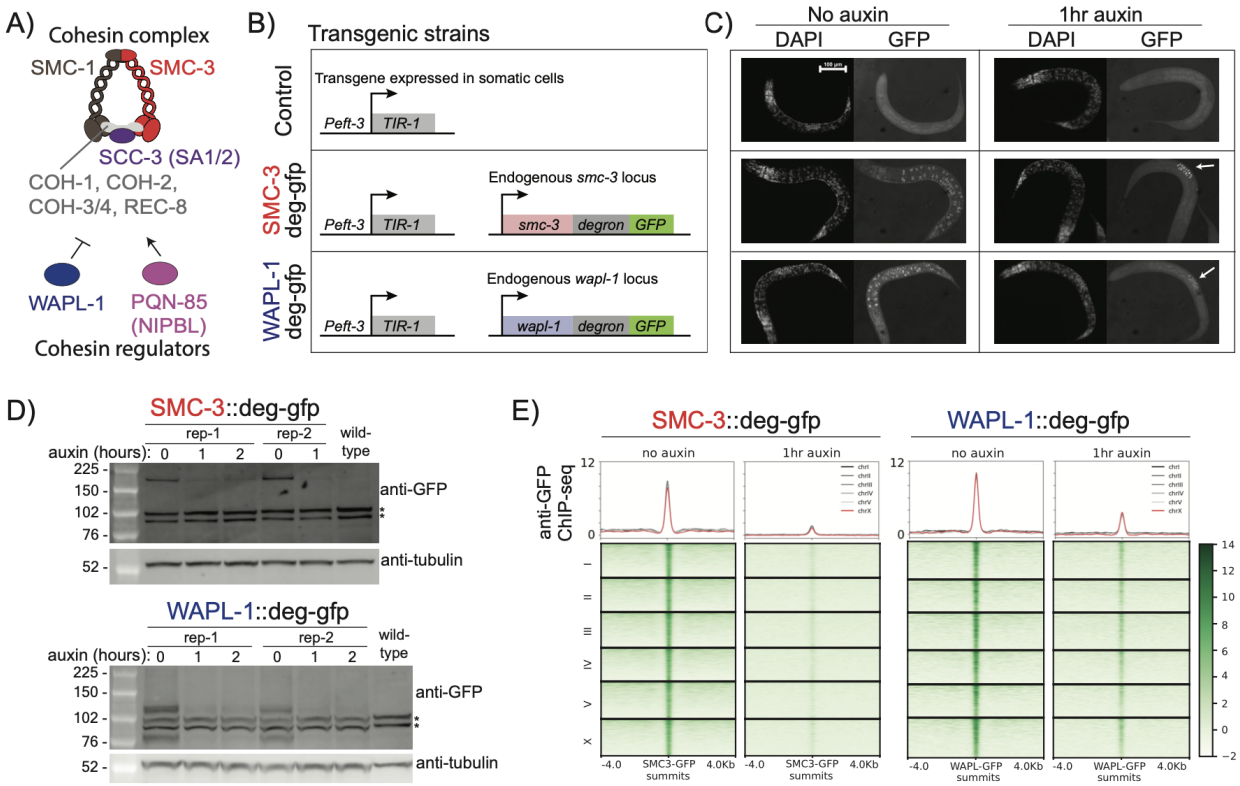

Figure 2. Acute depletion of cohesin and WAPL from somatic cells.
A) *C. elegans* subunits of cohesin and its regulators. B) Transgenic strains used in this paper. Exogenously inserted TIR1 is expressed in somatic cells using the *eft-3* promoter. Endogenous *smc-3* or *wapl-1* are C-terminally tagged with degron-gfp. C) DAPI and GFP images of L3 stage worms. White arrow indicates that the proteins in the germline are not degraded upon auxin treatment due to TIR1 presence only in the somatic cells. Scale bar: 100um. D) Western blot images of L3 stage worms with increasing auxin treatment duration. Anti-GFP antibody was used to show global depletion of the tagged protein. Anti-tubulin antibody was used as loading control. Asterisk indicates background bands. E) Meta-plot of ChIP-seq data grouped into different chromosomes. Anti-GFP antibody was used to show uniform depletion of SMC-3 and WAPL.

Distinct domains of cohesin binding extend upon WAPL depletion

In vitro, SMC complexes translocate along DNA (Hassler et al. 2018). *In vivo*, this dynamic process manifests in ChIP-seq signal track as 'spreading', where the enrichment gradually decreases with increasing genomic distance from a loading source (Brandao et al. 2019). In bacteria, insertion of *parS* sequences results in spreading of bacterial SMC complex (Sullivan et

al. 2009; Wang et al. 2017; Wang et al. 2018). In worms, an X-specific condensin surrounds its recruitment elements on the X (Anderson et al. 2019; Rowley et al. 2020; Kim et al. 2022; Morao et al. 2022). Targeted loading of cohesin using tetO-tetR system also showed spreading of cohesin binding at nearby CTCF sites (Han et al. 2023). Thus, observation of spreading implies the presence of loading sites.

In the control condition, we observe that cohesin binding shows a mix of peaks and background enrichment of ChIP-seq signal, creating cohesin bound-domains (Figure 3A, black panel). The example domain is ~30 kb in size and form over a highly transcribed region indicated by RNA Pol II ChIP-seq and GRO-seq. Importantly, the distance of cohesin binding is extended upon depletion of WAPL, suggesting cohesin spreads further from loading sites (Figure 3A, blue panel). Given that WAPL functions to suppress the residence time of cohesin on DNA, we conclude that the observed spreading reflects a dynamic process, whereby the distance traveled depends on the time cohesin resides on the DNA.

Cohesin binding domains emanate from NIPBL occupied sites

Upon SMC-3 depletion, residual amounts of SMC-1 can be detected in the middle of the spreading region (Figure 3A, red panel). Given that cohesin requires ATP hydrolysis to translocate *in vitro*, and that ATP hydrolysis requires heterodimerization of head subunits from both SMC-1 and SMC-3 (Hopfner and Tainer 2003; Muir et al. 2020), we speculate that the residual SMC-1 signal reflects the initial loading site for cohesin. The *C. elegans* ortholog of the cohesin loader NIPBL is encoded by the gene *pqn-85*/*scc-2*. Thus, we tested this idea by performing ChIP-seq for cohesin loader NIPBL in the control condition. ChIP-seq signal for NIPBL does not track cohesin spreading and resembles the binding pattern of the residual SMC-1 in SMC-3 depletion (Figure 3A). While whether NIPBL is a loader and processivity factor is still debated (Ciosk et al. 2000; Kagey et al. 2010; Alonso-Gil et al. 2023; Banigan et al. 2023; Han et al. 2023), the lack of spreading pattern in NIPBL track suggests that NIPBL functions as a loader rather than a processivity factor that moves with cohesin in *C. elegans* (discussed below after Hi-C analysis).

Next, we analyzed the shift in cohesin binding from control to WAPL depletion conditions. Upon WAPL depletion, cohesin binding is reduced within the control cohesin binding domains, while increasing outside (Figure 3A). Replicates of ChIP-seq data showed some variability in the extent to which cohesin moves outwards, suggesting that increased loop extrusion processivity has not reached steady-state after one hour of WAPL depletion (Supplemental Figure 1). Genome-wide, the number of cohesin binding sites (inferred from SMC-1 and SMC-3 peaks) are comparable, but distinct between control and WAPL depletion conditions (Figure 3B). Furthermore, the peaks that appear upon WAPL depletion are further from the nearest NIPBL binding sites (Figure 3C). Together, these results suggest that cohesin travels away from NIPBL sites with increasing residence time and support a model in which cohesin is initially loaded at a putative loading site occupied by NIPBL, from which cohesin spreads dynamically in bi-directional fashion.

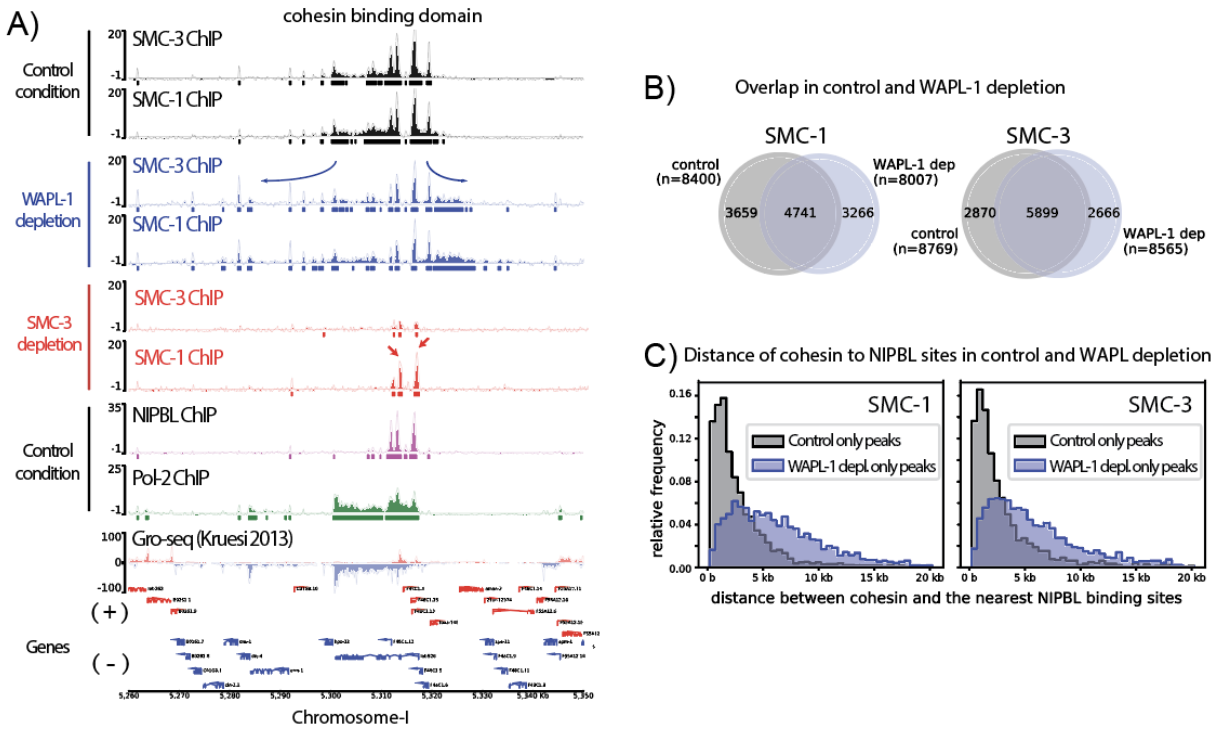

Figure 3. Cohesin spreads bi-directionally from putative loading sites.
A) Genome browser view of a cohesin enriched domain. Shown are cohesin binding (SMC-3 and SMC-1) in control condition (top black panel), WAPL depletion condition (blue panel), and SMC-3 depletion condition (red panel). NIPBL, RNA Pol II and GRO-seq (46) in control condition are shown below (bottom black panel). B) A second example illustrates two domains. One more diffuse with shorter and distributed NIBPL peaks (left) and the other with more focal and stronger NIBPL peaks (right). C) Venn diagram showing difference in cohesin binding sites inferred from MACS2 narrow peak-caller in control vs. WAPL depletion conditions. D) Relative frequency of distance between cohesin peaks to the nearest NIPBL binding sites. Only the control or WAPL depletion specific peaks were used to illustrate the increased distance of peaks in WAPL condition.

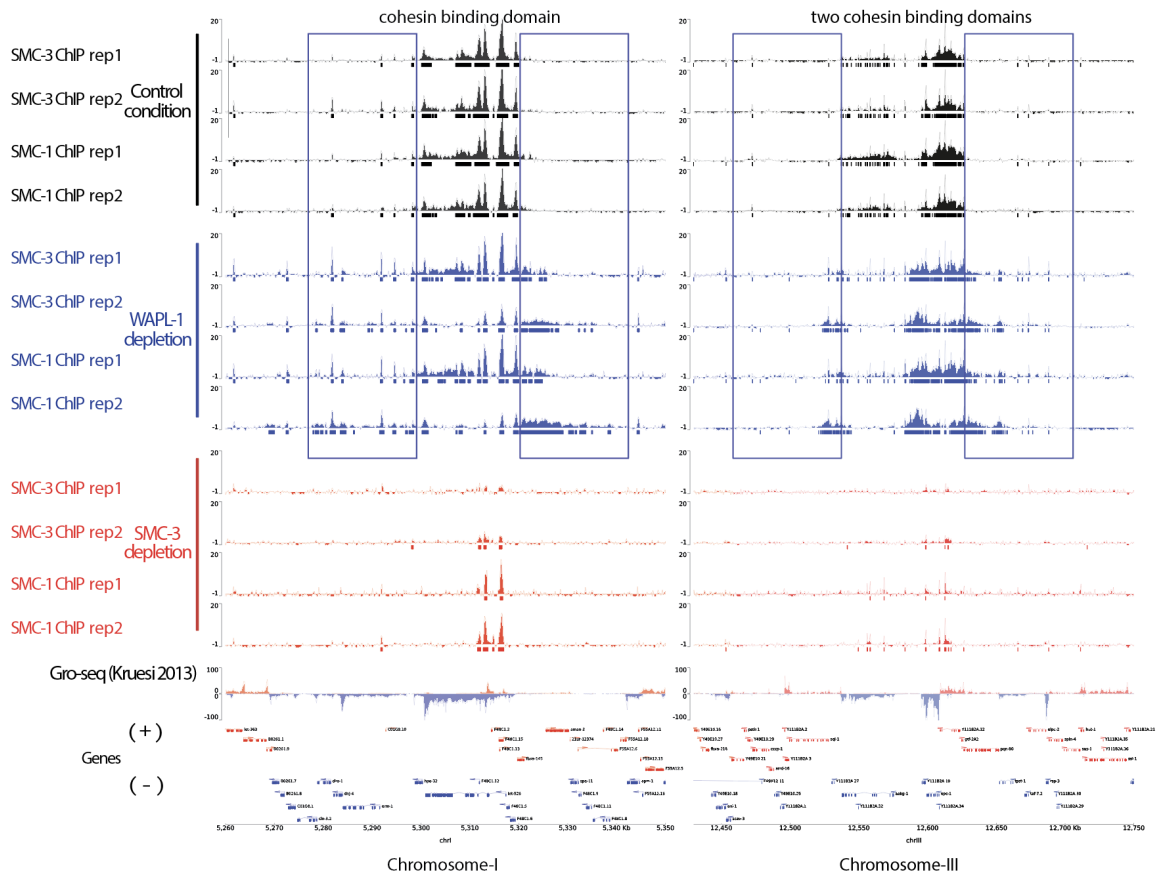

Supplemental Figure 1. Replicates of SMC-1 and SMC-3 ChIP-seq data in control, SMC-3 and WAPL depletion conditions.
Genome browser view of ChIP replicates corresponding to representative regions in main figures. Rectangles are drawn to highlight the outward translocation of cohesin upon WAPL depletion.

Bi-directional loop extrusion by cohesin forms chromatin jets detected by Hi-C

In vitro, cohesin performs two-sided loop extrusion (Davidson et al. 2019; Kim et al. 2019). In simulation, cohesin was inferred to be an *effectively* two-sided loop extruding factor based on Hi-C data (Banigan et al. 2020). *In vivo*, recent observation of chromatin jets or plumes further supports cohesin as a two-sided loop extruding factor (Liu et al. 2021a; Guo et al. 2022; Galitsyna et al. 2023; Isiaka et al. 2023). DNA-damage induced recruitment of cohesin or artificial loading of cohesin via a tetO-tetR system generated 'stripe', suggesting that cohesin could also act as a one-sided loop extruding factor (Arnould et al. 2021; Han et al. 2023). Our population average ChIP-seq data (Figure 3) cannot distinguish whether the spreading of cohesin towards left and right occur simultaneously, which would imply two-sided loop extrusion, or independently, which would imply one-sided loop extrusion. Thus, we performed Hi-C to distinguish between the two different underlying behaviors of cohesin.

In the control condition, we observe a short chromatin jet (Figure 4A, left) at the example region presented in Figure 3A. In the SMC-3 depletion, the jet is lost, indicating that the jet is cohesin

dependent (Figure 4A, center). In the WAPL depletion condition, where cohesin spreads farther, the jet is extended, suggesting that cohesin initially forms a smaller loop and then a larger loop with increasing residence time on DNA (Figure 4A, right). Consistent with ChIP-seq data showing that cohesin spreads farther towards left than right (SMC-3 ChIP-seq track below Hi-C data), the jet shows left-ward tilt (Figure 4A). Our Hi-C data suggests that loop extrusion by cohesin is effectively two-sided.

Chromatin jet origins coincide with strong NIPBL binding

ChIP-seq analysis of cohesin binding and the resulting chromatin jets suggest that cohesin is preferentially loaded at the jet origins. We define jets as a segment of DNA that have locally enriched contacts near the main diagonal that reduces upon cohesin depletion and shows a peak in control and WAPL depletion (Supplemental Figure 2A). The 'jet strength' is calculated from the peak prominence of insulation score from control-cohesin conditions, thus measuring cohesin dependence. Meta analysis of average Hi-C signal in quartiles of jet strength confirmed the identification of cohesin dependent chromatin jet origins (Figure 4B) and was consistent between experimental replicates (Supplemental Figure 2B).

If jets are formed by focal loading of cohesin by NIPBL, jet origins and strength should correlate with NIPBL binding. Indeed, the strength of the jet positively correlated with both average NIPBL ChIP-seq signal (Figure 4C) as well as the number of NIPBL peaks (Figure 4D). We also considered the alternative idea that rather than preferential loading at NIBPL sites, the observed cohesin binding at the jets is a reflection of stalling. In the bacterial and mammalian systems, RNA polymerase II functions as a moving barrier for loop extrusion (Brandao et al. 2019; Banigan et al. 2023). Two Hi-C features were reported to reflect the barrier effect of RNA Pol II but are not detected in our data. We observed no broad 'stripe' originating from the transcribed gene body that would be predicted if cohesin is stalled by broadly distributed RNA Pol II along the gene body, and no insulation effect across the gene body as cohesin fails to facilitate contacts across. Instead, interaction across the cohesin spreading region is facilitated, not insulated (Figure 4A, see insulation score increase across the SMC-3 binding region). Thus, cohesin enrichment at jets reflects increased loading rather than stalling. Together, our results suggest that preferential loading of cohesin followed by bi-directional loop extrusion form chromatin jets (Figure 4E).

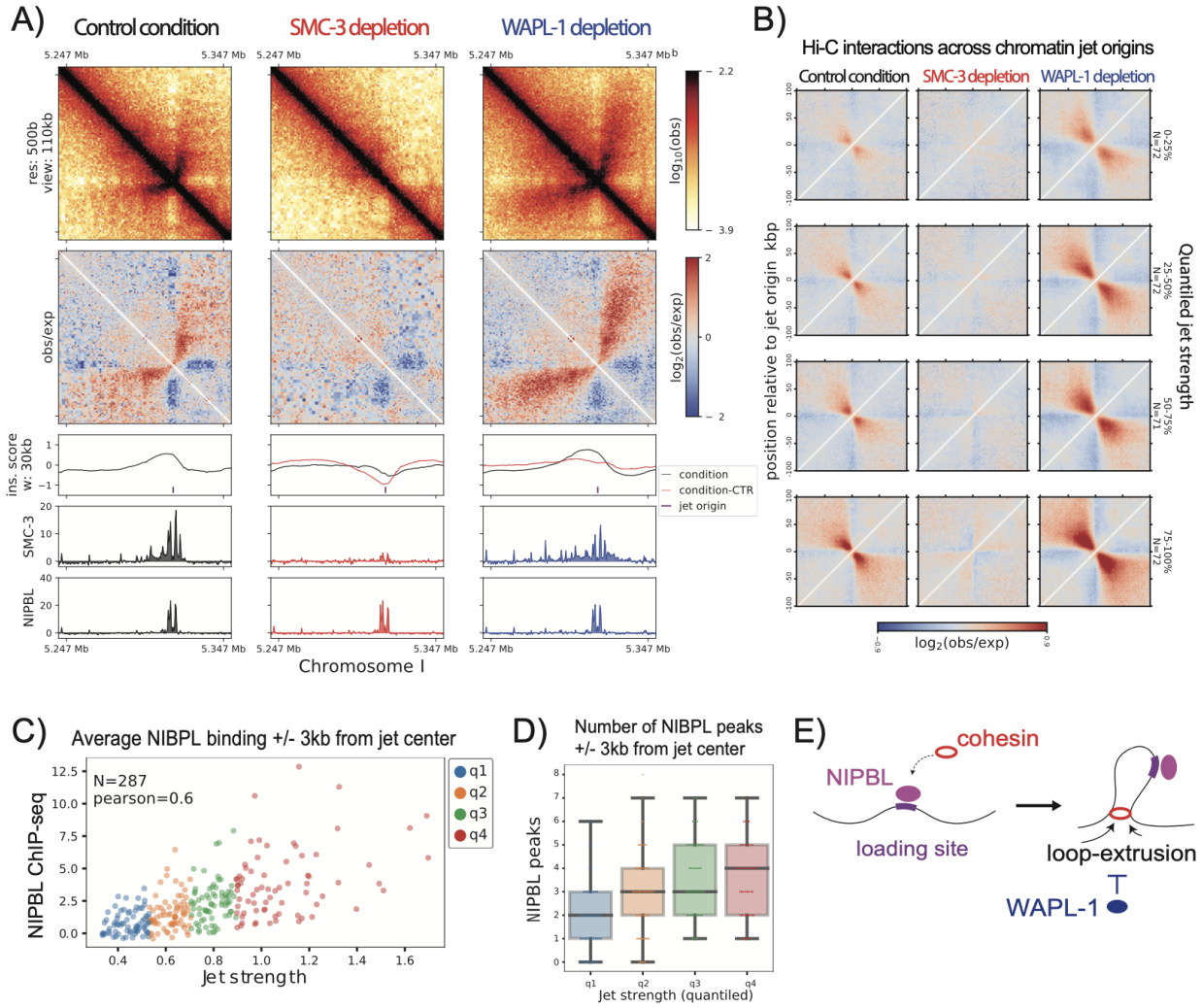

Figure 4. Bi-directional spreading of cohesin forms chromatin jets
A) Hi-C snapshot of the cohesin binding domain shown in Figure 2A in control, SMC-3 and WAPL depletion conditions. Going from the top to bottom row: The observed balanced matrix, distance-decay normalized observed-over-expected matrix, insulation score using 30kb-window and 500bp-step (black lines – condition (control of depletions), red lines – condition minus the control), and cohesin ChIP-seq data are plotted. Both Hi-C and ChIP-seq data are binned over 500bp. The jet origins inferred from Hi-C data are marked as purple vertical ticks with insulation scores. Total of 287 jets are identified using Hi-C data. B) On-diagonal pileup of observed-over-expected matrix centered at jet origins quantiled based on the jet strength for three conditions. C) Scatter plot of jet strength vs. NIPBL ChIP average signal over 6kb region in control condition. The jet strength corresponds to peak prominence in the Hi-C insulation score change upon cohesin knockdown (control minus SMC-3 depletion). D) Boxplot of jet strength (divided into four equal groups) and the number of called NIPBL peaks. E) Cartoon model depicting bidirectional loop extrusion by cohesin forming jets.

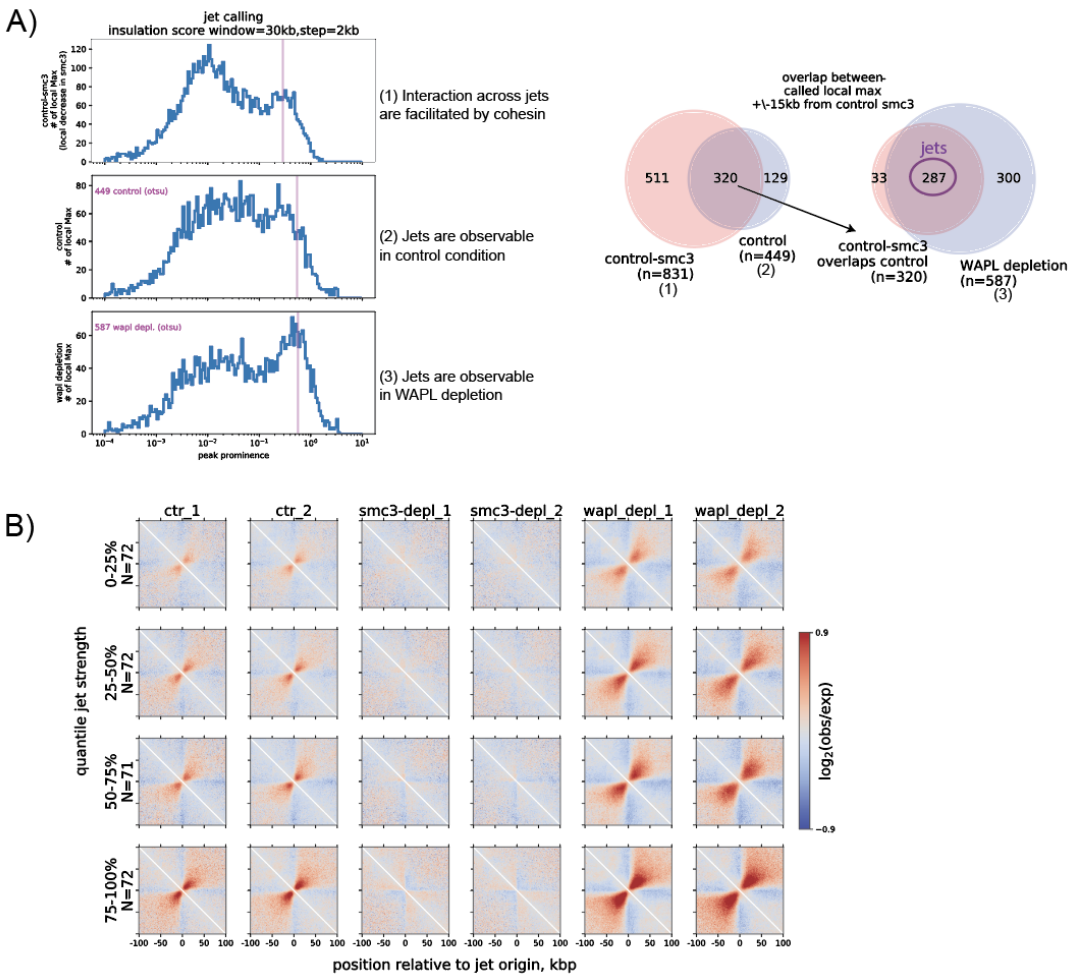

Supplemental Figure 2. Jet calling method
A) Left panel) Histogram of local maxima with varying degree of peak prominence. We reason that identified 'jets' must be (1) facilitated by cohesin, (2) observable in control condition, and (3) observable in WAPL condition. These three conceptual criteria are applied computationally as identifying significant local maxima of (1) insulation scores delta (control condition minus SMC3 depletion condition), (2) insulation scores in control condition, and (3) insulation scores in WAPL depletion condition. The 'jet strength' in Figure 3C,D is the peak prominence of insulation scores delta (1), ie. the strength of interaction facilitated by cohesin. The significant local maxima are called based on Otsu's method of signal-noise separation. Right panel) Pair-wise overlap between significant local maxima called from above criteria. Due to shift in the maxima occurring from tilt of the jets, the 'overlap' allows for +/-15kb maximum distance (half of the insulation score window) from the local maxima called by insulation delta (1). We reason that insulation delta (1) provides the most accurate position and strength of the jet origin since it corrects for underlying Hi-C structure that is not cohesin dependent. B) On-diagonal pileup of observed-over-expected matrix for each replicate is centered at jet origins quantiled based on the jet strength for three conditions.

Chromatin jet patterns are influenced by surrounding loading sites that lead to clashing and stalling of cohesin molecules

Analyses of Hi-C patterns upon WAPL depletion suggest that loading and clashing of cohesin complexes determine the structure and trajectory of the chromatin jets. Broad loading of cohesin was proposed to create domains of increased 3D contacts with extension from the diagonal (Guo et al. 2022). Indeed, we observed that at a cohesin binding domain with broad NIPBL binding, the diagonal Hi-C interactions were further extended upon WAPL depletion, supporting that this particular chromatin jet is formed by cohesin molecules loaded over a broad region (Figure 5A).

In the genomic region with two cohesin binding domains, Hi-C analysis upon WAPL depletion suggests clashing of cohesin molecules (Figure 5B). The cohesin domain on the left is marked by lower cohesin ChIP-seq signal and small but numerous NIPBL peaks distributed over a wider region (Figure 5B). The domain on the right is marked by stronger and more focal NIPBL binding. Upon WAPL depletion, the resulting Hi-C pattern suggests that the cohesin molecules originating from the two domains stall in the middle, while continually extruding on the opposing sides (Figure 5B). This creates diffuse stripes emanating from the putative sites of stalling and increases contacts between the two loop domains further away from the main diagonal.

In summary, the loading of cohesin at jet origins occur at a high frequency such that the two cohesins loaded at two closely located genomic locations often run into each other resulting in a domain-like structure if the loading sites are broad/clustered (Figure 5A), or in a jet-to-stripe transition if the two loading sites are separated by a short distance (Figure 5B). Therefore, the resulting patterns of cohesin-mediated Hi-C contacts and the structure of chromatin jets is genomic context dependent and largely controlled by the distribution of cohesin loading sites.

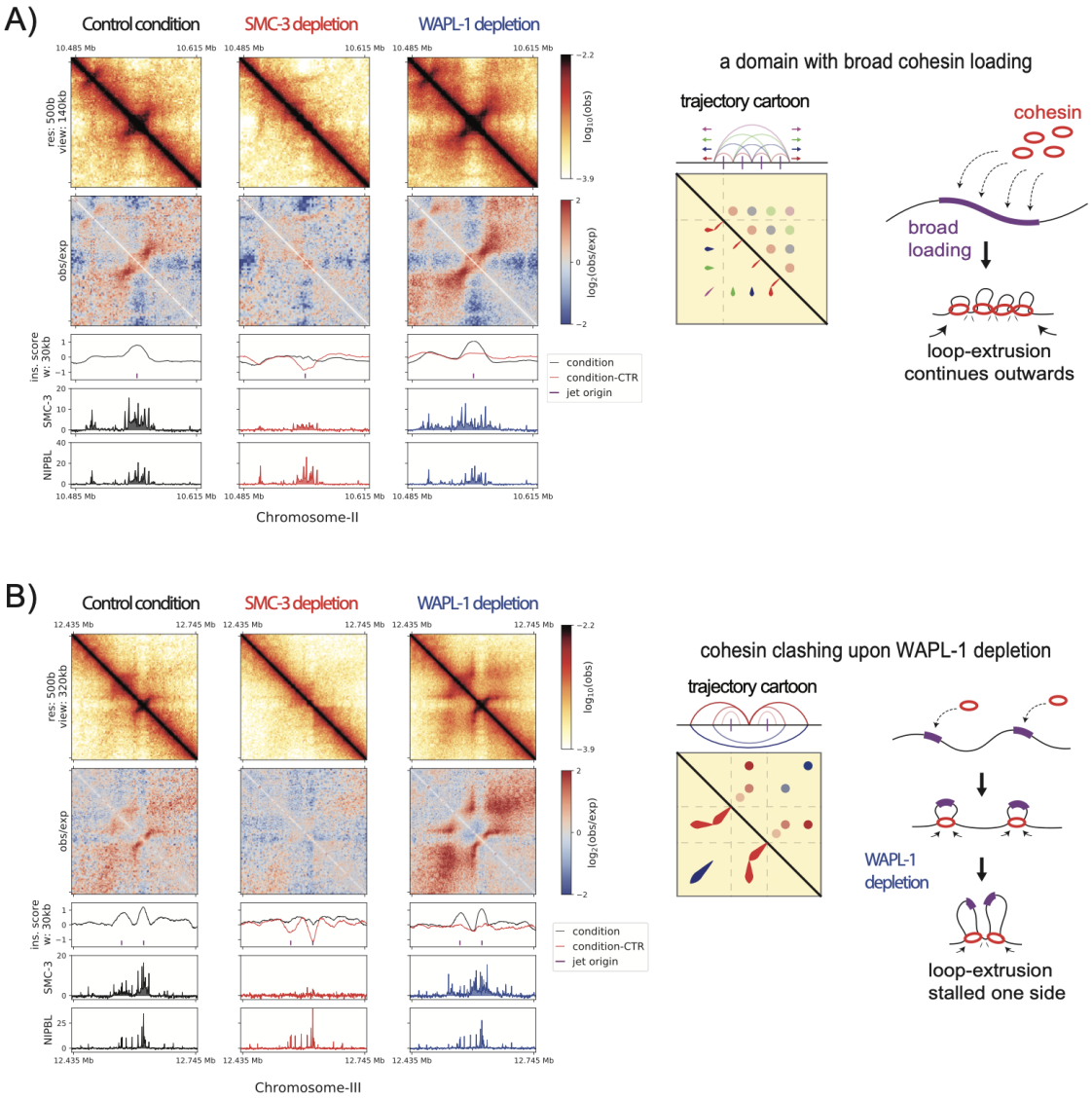

Figure 5. The pattern of chromatin jets is influenced by the distribution of loading sites. A) Hi-C snapshot of a locus containing broadly distributed cohesin. Cartoon showing highly clustered loading events leading to cohesin-cohesin collisions, leading to domain-like patterns. SMC-3 (black), NIPBL (purple) ChIP-seq tracks for control conditions are shown. B) Hi-C snapshot of a locus containing two separated and closely located cohesin domains. Cartoons showing the jet trajectory of two cohesin looping events leads to collision, which in turn leads to stalled one-sided loop extrusion and formation of secondary enriched contacts away from the main diagonal (blue trajectory in the cartoon).

Cohesin and WAPL depletion does not affect NIPBL binding

NIPBL orthologs were identified as a loading factor with its interacting partner SCC-4 in several species including *C. elegans* meiosis (Seitan et al. 2006; Lightfoot et al. 2011). NIPBL was also proposed to be a processivity factor that travels with cohesin in the mammalian systems (Davidson et al. 2019; Kim et al. 2019; Alonso-Gil et al. 2023; Banigan et al. 2023). We reasoned that if cohesin mediates NIPBL crosslinking to chromatin, a portion of NIPBL sites

must be SMC-3 dependent. This prediction was not met. Unlike SMC-1, NIBPL binding did not change upon SMC-3 depletion (Figure 6A). SMC-1 ChIP-seq signal was reduced and narrowed across the jet origins, but NIBPL signal did not alter (Figure 6B). Furthermore, upon SMC-3 depletion, persisting SMC-1 ChIP-seq peaks were closer to the jet origin, but NIPBL peaks position did not change (Figure 6C). Thus, acute depletion of SMC-3 depletion does not affect NIPBL binding.

A second prediction of NIPBL translocating with cohesin is that upon WAPL-1 depletion, NIPBL binding should also increase outwards from the jet origins. However, this does not unequivocally refute a recruitment-function (defined as proteins whose absence eliminates binding of SMC to loading sites), because known recruiters of SMC complexes such as bacterial parB and SDC proteins also spread beyond the loading sites in the presence of the SMC complexes (Ercan et al. 2009; Graham et al. 2014; Kim et al. 2022). This apparent spreading may be due to stable physical interaction between the recruiters and the SMC complexes during loop extrusion or DNA looping crosslinking the recruiter protein to sites of spreading as measured by ChIP-seq.

Regardless, we performed NIPBL ChIP-seq upon one hour of WAPL-1 depletion (Figure 6A). To account for biological variation in processivity of cohesin upon WAPL depletion, we compared NIPBL and SMC-3 binding in the same ChIP extracts (Supplemental Figure 3). Unlike SMC-3, NIPBL binding did not extend outward from the chromatin jet origins (Figure 6B). Consistently, the distance between jet origins and NIPBL binding peaks did not differ between the control and WAPL-1 depletion conditions (Figure 6C). Thus, NIPBL distribution does not change upon WAPL depletion. Together, these results show that NIPBL binding is not cohesin dependent in *C. elegans*.

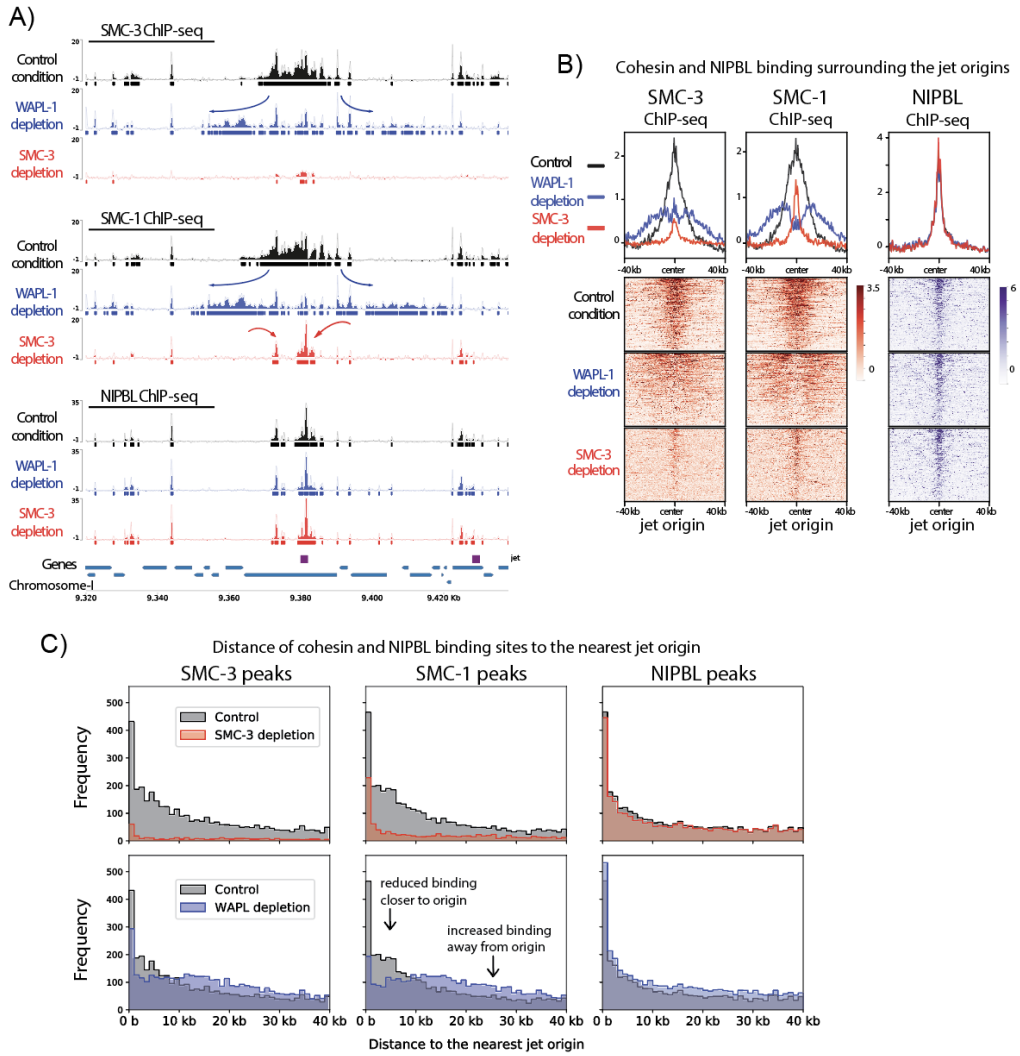

Figure 6 NIPBL does not spread with cohesin and is binding is independent of cohesin
A) Genome browser view of SMC-3 (top panel), SMC-1 (middle panel), and NIPBL (bottom panel) ChIP-seq profiles in control (black), and SMC-3 (red) and WAPL (blue) depletion (red) conditions. B) Metaplots of SMC-3, SMC-1, and NIPBL ChIP-seq scores centered at the jet origins for control (black), SMC-3 (red) and WAPL (blue) depletion (red) conditions. and SMC-3 depletion (red) conditions. C) Histogram of distance between the nearest jet origins and the binding sites of SMC-3, SMC-1, and NIPBL, under control (gray) and SMC-3 depletion (red) conditions. D) Histogram of distance between the nearest jet origins and the binding sites of SMC-3, SMC-1, and NIPBL, under control (gray) and WAPL depletion (blue) conditions.

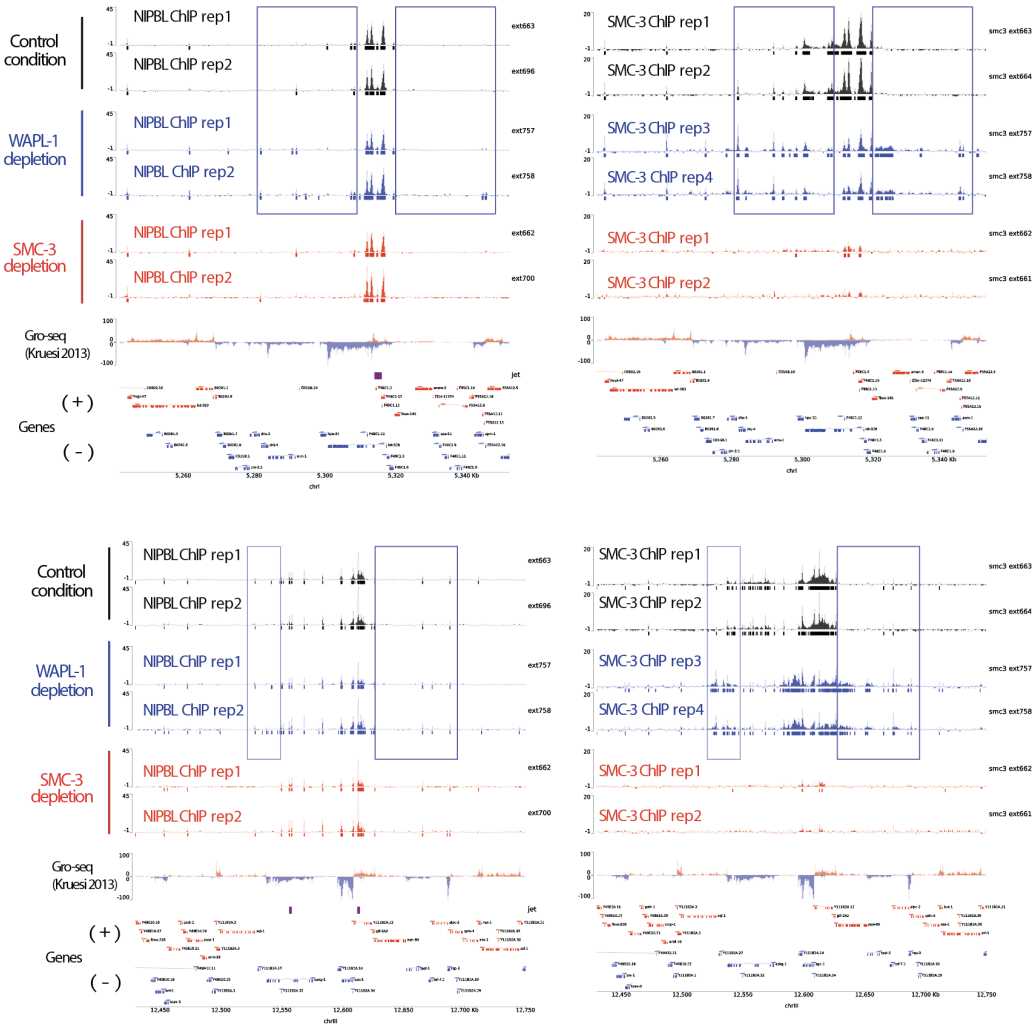

Supplemental Figure 3. Replicates of NIPBL ChIP-seq data in control, SMC-3 and WAPL depletion conditions.
NIPBL ChIP-seq tracks for the control, WAPl-1, and SMC-3 depletion conditions (left) compared to the SMC-3 ChIP-seq tracks in the same conditions (Right). Two different regions are shown. On the top is the same region as in Figure 3A and on the bottom the region in Figure 5B. The ChIP extract identification numbers are provided to compare the effect of WAPL depletion on SMC-3 and NIPBL in the same ChIP extract and account for biological variability. The rectangles are used to highlight regions outside the cohesin binding domains in control regions where SMC-3 binding spreads out to in WAPL depletion. The same regions did not show increased NIPBL binding highlighting that unlike SMC-3 NIPBL localization is not dependent on WAPL.

Cohesin-mediated DNA loops in C. elegans are shorter than those observed in mammals

While the jets are pronounced Hi-C features, they may reflect above-average cohesin behaviors on chromatin. The contact probability curve, P(s), and its log-derivative are powerful metrics for estimating the average loop size of the chromosome (Gassler et al. 2017; Polovnikov et al. 2023). In the mammalian system, cohesin forms 100-200 kb loops on average (Davidson et al. 2019;

Polovnikov et al. 2023), while the jets can propagate up to 1 to 2 Mb (Guo et al. 2022). Here, we use the similar metric to infer cohesin loop size. While we do not observe a local maximum in the log-derivative of P(s) that disappears in the SMC-3 depletion condition, we observe a more pronounced local minima in the SMC-3 depletion condition. We use this to infer that cohesin makes loops of size 15.7 kb (Figure 7A). In the WAPL depletion, a local maximum is readily observed, indicating that cohesin makes more extended loops of size 25 kb (Figure 7A). These numbers are smaller than the length of exemplary jets, which can extend up to ~50kb (Figure 3, 4). On the X chromosome, activity of a dosage compensation specific condensin forms TADs and represses transcription (Albritton and Ercan 2018; Kim et al. 2022). Interestingly, the cohesin mediated DNA loops are shorter on the X compared to autosomes (Figure 7A). We conclude that average *C. elegans* cohesin loops are ~10 fold smaller than the ones formed by the mammalian cohesin and chromatin jets may be formed by cohesin molecules with higher-than-average processivity.

Chromatin jets correlate with transcription

Across the genome, jets coincided with domains of highly transcribed genes. Plotting GRO-seq enrichment (Kruesi et al. 2013) over jet origins showed a positive correlation between jet strength and transcription (Figure 7B). Notably, strong and continuous transcription often pointed away from the origins of strong jets in either direction, suggesting that cohesin and RNA Pol II translocate in the same direction (Figure 7B). The example jet shown in Figure 3A tilted to the left and cohesin processivity correlated with a long-transcribed gene in the same direction (Supplemental Figure 4A). Our jet calling is based on the strength of square domain facilitation and does not measure tilt. To take shape into account, we applied a recently published method called Fontanka (Galitsyna et al. 2023).

A significant proportion of chromatin jets (219 out of 287) were also detected by Fontanka using shapes of three different masks (Supplemental Figure 4B). We identified 262 and 249 left and right fountains using the left and right masks, respectively. And of these, 77 and 62 fountains were called mutually exclusively as defined by no oppositely tilted fountain in +/-50kb range (Figure 7C). If there is a correlation with the tilt of a jet and the direction of transcription, left and right tilted jets should show an enrichment of “minus” and “plus” GRO-seq coverage, respectively. There was weak correlation between the tilt of a jet and the direction of transcription surrounding the jet origin (Figure 7D). Individual examples suggest that the influence of genes transcribed in opposing directions and the presence of numerous cohesin loading sites may reduce the simple correlation we sought between transcription and cohesin processivity (Supplemental Figure 4C). Nevertheless, the correlation between jet strength and transcription level and direction (Figure 7B) indicate that the strong jets are formed at regions where cohesin and transcription frequently travel in the same direction (Figure 7E).

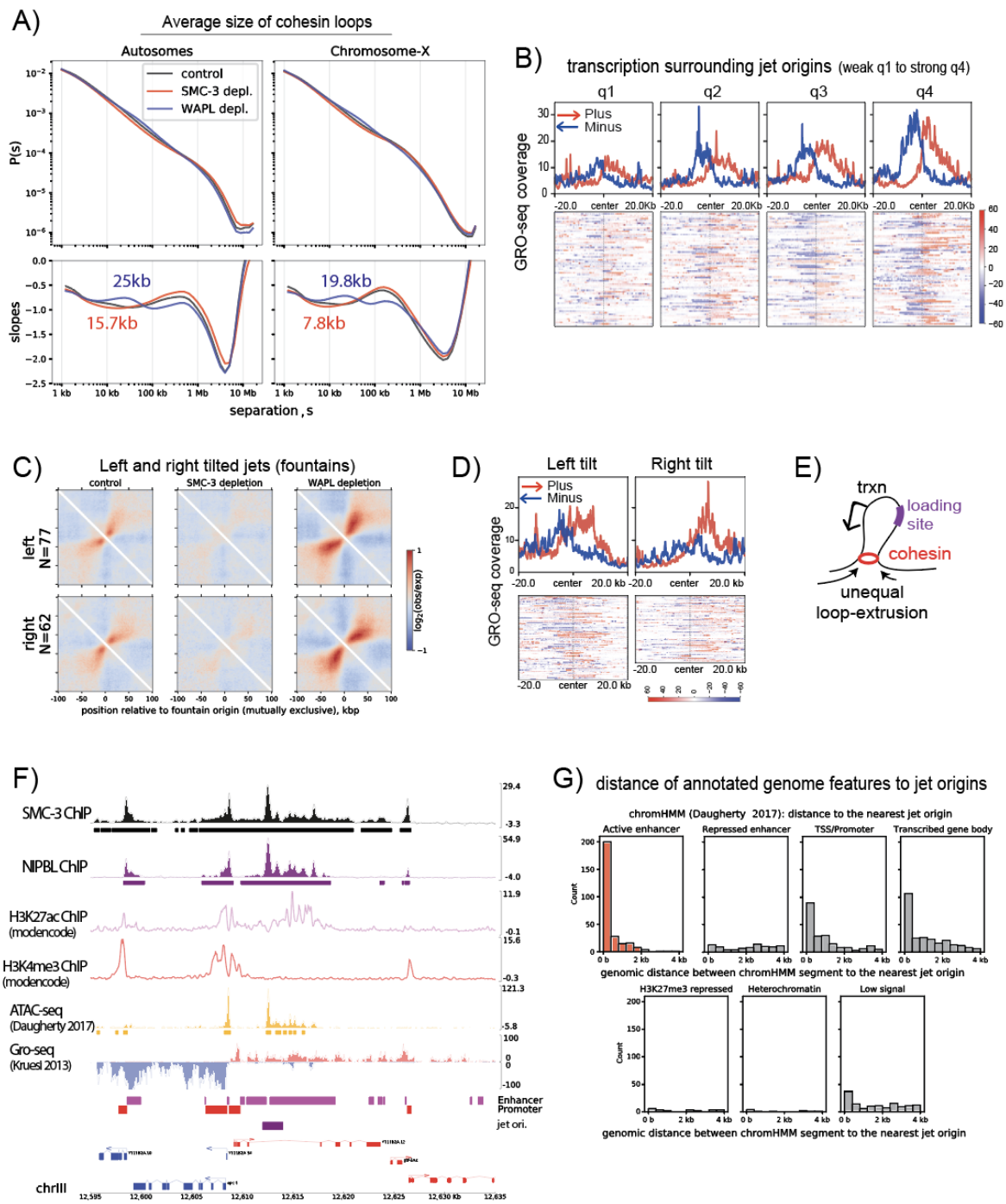

Figure 7. Correlation between transcription and chromatin jets

A) Contact probability, P(s), as a function of linear genomic separation between pairs of loci, s (top row), and its log-derivative, the slopes of P(s) in log-space, (bottom row) are plotted for three conditions in different colors. The inferred average loop size for cohesin in unperturbed state (red arrow) and the extended average loop size for cohesin in WAPL depletion condition (blue arrow) are annotated. B) Gro-seq data from (Kruesi et al. 2013) are plotted across jet origins categorized into four quantiles based on the jet strength. Blue track indicates minus

strand and the red track indicates plus strand. The order of rows in the heatmaps for plus and minus tracks are identical. The strength of jet origins correlates with the strength of transcription. The jet origins tend to be located at the start of transcribing segments. C) Fountains detected by Fontanka (Galitsyna et al. 2023) were categorized as having a left or right tilt (center). D) Gro-seq data from (Kruesi et al. 2013) are plotted across fountain origins categorized as left or right tilted. Blue track indicates minus strand and the red track indicates plus strand. The heatmaps were juxtaposed to highlight the transcription direction surrounding the fountain origins. E) Genome browser view of an example chromatin jet origin with distinct enhancers and promoters marked by H3K27ac and H3K4me3. F) Histogram of 1kb binned genomic distance between identified jet origin in this paper and the annotated regions of chromHMM in (51). G) At chromatin jets cohesin and transcription (indicated with an arrow) often translocate towards the same direction.

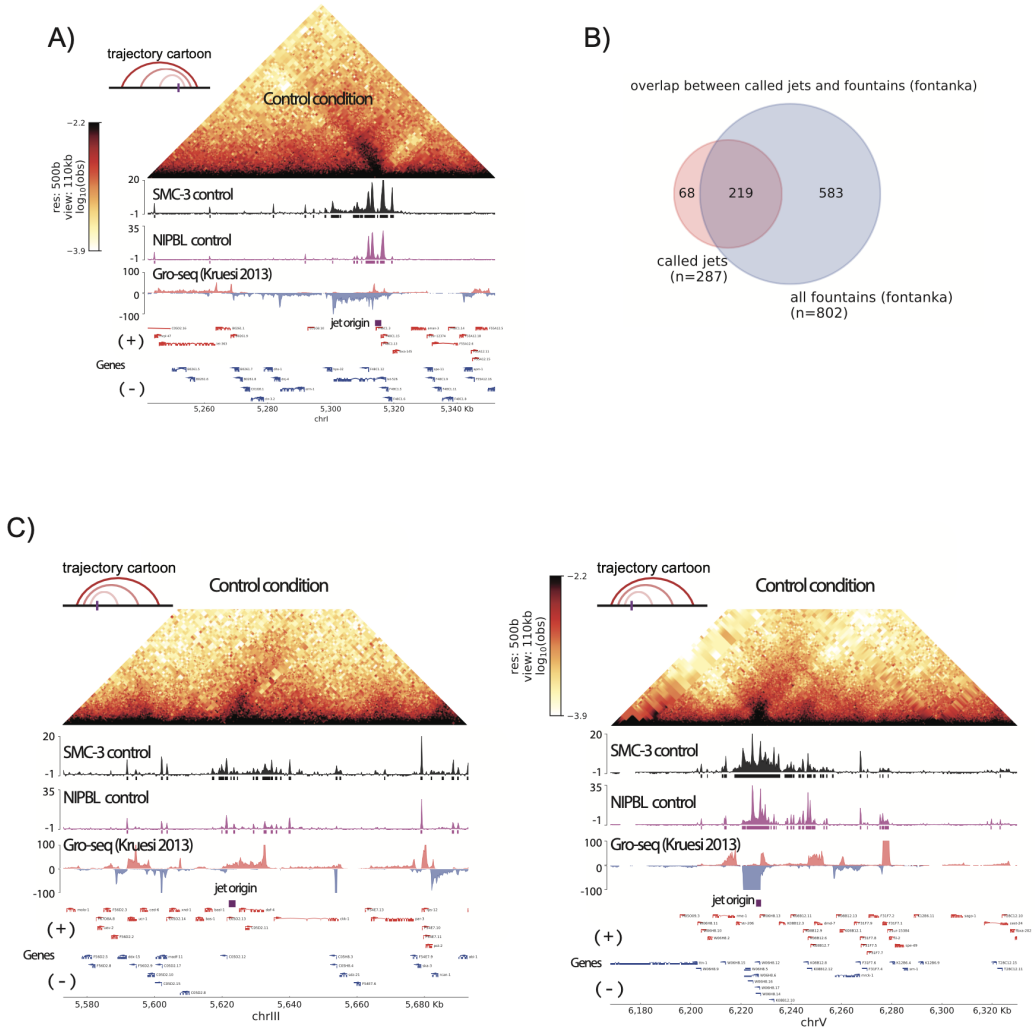

Supplemental Figure 3. Correlation between jet tilt and transcription
A) The example jet region (also highlighted in Figure 2A and 3A (skewed to the left and correlated with transcription. GRO-seq, NIPBL, and SMC-3 ChIP-seq tracks are plotted across the Hi-C map. B) Fountains detected by Fontanka were categorized as Hi-C interactions across the fountains that were categorized as having a left or right tilt (center). Overlap (+/- 10 kb)

between jets and fountains identified by Fontanka (Galitsyna et al. 2023). C) Hi-C map of two jets shown with GRO-seq, NIPBL, and SMC-3 ChIP-seq tracks data plotted across the same example region. The jet origins are located at the upstream regions of transcribed genes. The longer range 3D DNA contacts of each jet was identified as skewing to the right. On the left panel, the right tilt of the jet correlated with a long gene transcribed to the right. The jet on the right panel was also identified as "right-tilted", but the stronger transcription juxtaposing the origin was to the left. Therefore the direction of transcription juxtaposing a jet origin is not sufficient to explain tilt but may be the cumulative effect of the genes further down the focal cohesin binding and incoming cohesin from the neighboring cohesin loading sites.

Chromatin jet origins are close to active enhancers

Across the genome, cohesin and NIPBL binding correlated with accessible chromatin and histone marks associated with active promoters and enhancers (Figure 7F) as well as the two topoisomerases (Supplemental Figure 5A). Although *C. elegans* genome is compact, we were able to find regions where H3K27ac enriched enhancers were sufficiently distant from H3K4me3 enriched promoters and noticed that the jet origins were closer to the enhancers (Figure 7F). To analyze this overlap genome-wide, we compared the jet origins to genome annotations from two previous studies (Evans et al. 2016; Daugherty et al. 2017). Genomic regions designated as active enhancers by Daugherty et al. were closer to jet origins compared to other annotations (Figure 7G). Evans et al. split active enhancers into intergenic and intragenic (Supplemental Figure 5B). Together, these results suggest that cohesin loads at enhancers at higher frequency than other regions of the genome.

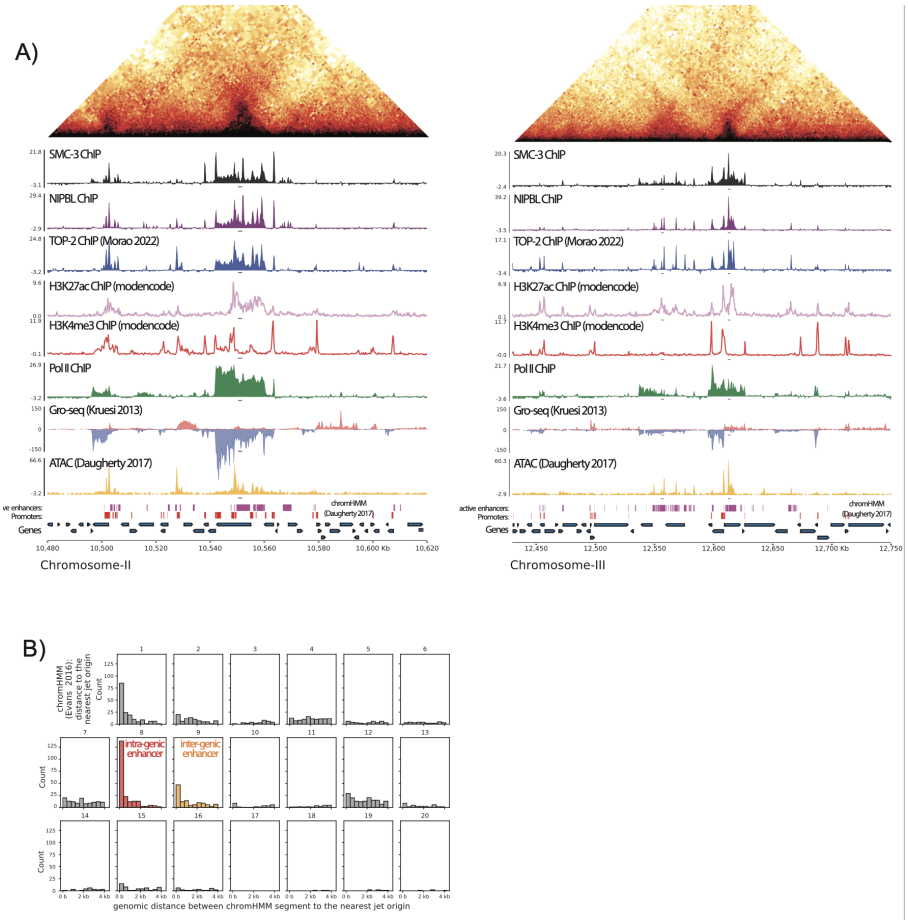

Supplemental Figure 4 Genomic features surrounding chromatin jet regions
A) Two representative regions are shown on the left and right and correspond to jets in Figure 5. Signal tracks and annotation for the region shown in panel A. SMC-3 (black), NIPBL (purple), TOP-2 (blue), H3K27ac (pink), H3K4me3 (red), and RNA Pol II (green) ChIP-seq tracks for control conditions are shown. Below are GRO-seq (Kruesi et al. 2013) and ATAC-seq (Daugherty et al. 2017) tracks and the annotated enhancer and promoter regions of chromHMM. B) Histogram of 1kb binned genomic distance between identified jet origin in this paper and the annotated regions of chromHMM in (Evans et al. 2016). Abbreviated annotation from the original paper: 1-Promoter, 2-7 transcription elongation body, 8-intronic enhancer, 9-intergenic enhancer, 10-weak enhancer, 11-border, 12-20-low expression and/or repeats.

One hour depletion of SMC-3 or WAPL does not lead to changes in RNA Pol II binding

We used RNA Pol II ChIP-seq analyses to analyze the effect of reduced cohesin in SMC-3 depletion and ectopic cohesin binding upon WAPL knockdown. Unlike the striking changes observed in Hi-C, cohesin and WAPL depletion did not result in significant change in RNA Pol II binding (Figure 8A). This observation was consistent across replicates (Supplemental Figure 6A). Unlike SMC-3, there was no detectable change in average RNA Pol II binding surrounding jet origins between control condition and SMC-3 and WAPL knockdown (Figure 8B)

To analyze the effect genome-wide, we categorized genes as being highly bound by cohesin in control compared to WAPL depletion (cohesin^{high} in control, aka control^{high}) or vice versa (cohesin^{high} in WAPL depletion, aka wapl dep.^{high}). Consistent with increased spreading of cohesin in WAPL depletion, genes designated as cohesin^{high} in control condition were closer to jet origins compared to those designated cohesin^{high} in WAPL depletion (Figure 8C). Validating gene categorization, SMC-3 ChIP-seq signal across the transcription start and end sites of genes bound highly by cohesin in control and WAPL depletion conditions decreased and increased, respectively (Figure 8D left panel). RNA Pol II did not follow the pattern of cohesin. RNA Pol II ChIP-seq signal did not change upon SMC-3 or WAPL depletion across the jet origins and was not different for the two categories of genes in either condition (Figure 8D right panel). These results suggest that cohesin is neither required for the maintenance nor sufficient to strongly regulate transcription in one-hour timescale.

SMC-3 or WAPL depletion causes subtle effects on mRNA-seq expression

To test if mRNA-seq analyses could capture differences in transcription compared to RNA Pol II ChIP-seq, we analyzed mRNA levels in larvae after 1 and 4 hours of SMC-3 and WAPL depletion. The average expression of genes closer to the jet origins (control^{high}) slightly reduced after one-hour of auxin mediated SMC-3 or WAPL-1 depletion compared to no-auxin condition (Figure 8E). To test if longer depletion would cause a stronger effect, we repeated the mRNA-seq analysis. To control for the potential effect of keeping worms for longer on auxin-containing plates without food, we used no-tag control strain in parallel. Four-hour auxin treatment did not show a difference on average expression (Supplemental Figure 6B). Therefore, we conclude that acute depletion of cohesin and WAPL immediately and dramatically change cohesin binding and the 3D DNA contacts measured by Hi-C, but do not result in equally strong changes in gene expression.

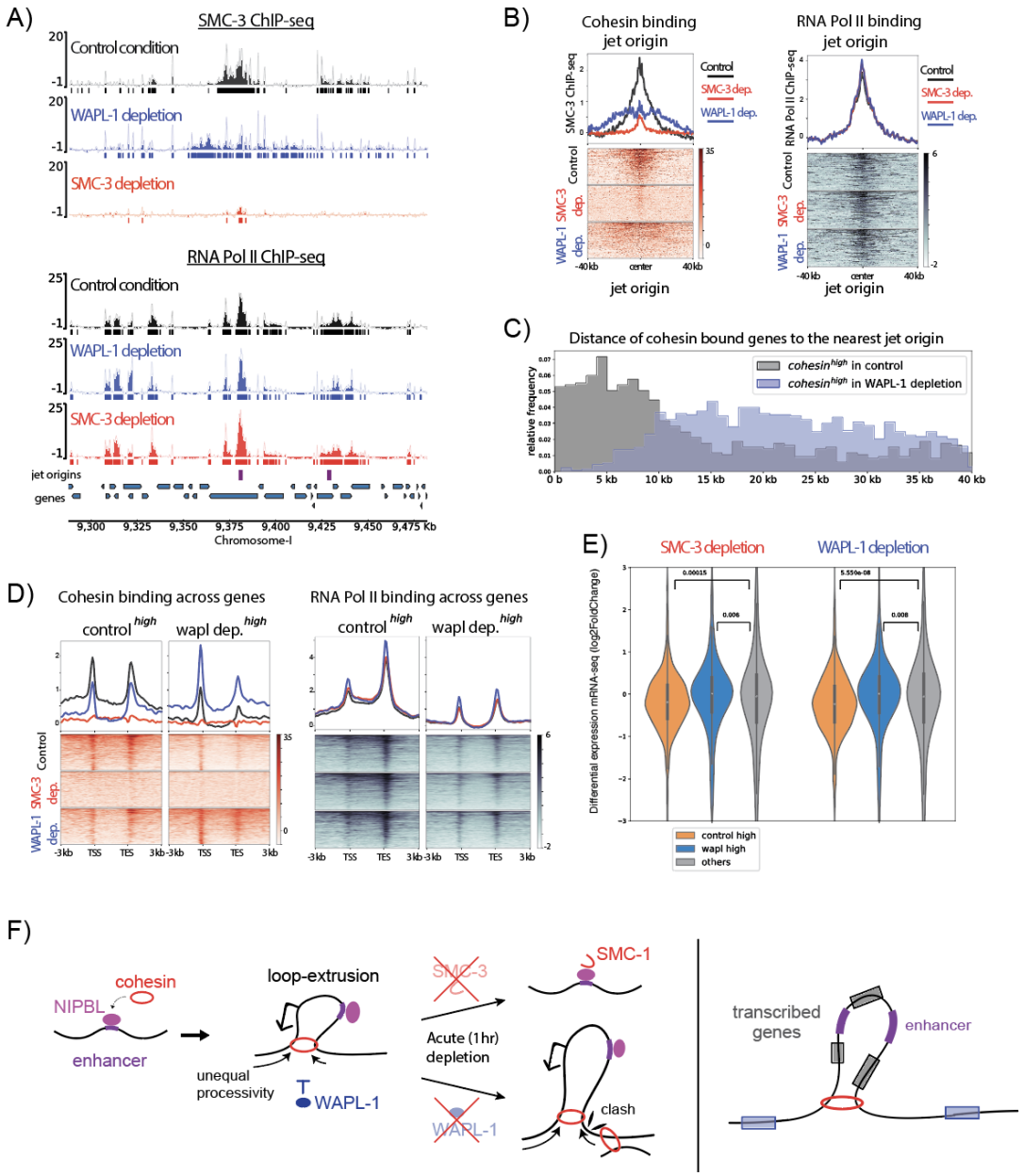

Figure 8 Acute depletion of cohesin and WAPL does not change RNA Pol II binding
A) Top panel: SMC-3 ChIP-seq track for the control, WAPl-1, and SMC-3 depletion conditions at an example region. Bottom panel: RNA Pol II ChIP-seq tracks for the same conditions and region. B) Shown are metaplots of SMC-3 and RNA Pol II ChIP-seq data centered at the jet origins. C) Genes are categorized as cohesin^{high} in control (black) or in WAPL depletion (blue) if the gene contains SMC-3 binding determined by MACS2 in the control condition and has higher average enrichment than in the WAPL depletion condition, and vice versa. The genomic distance between the genes and the nearest jet origins are calculated and plotted as 1kb-binned histogram. D) SMC-3 and RNA Pol II ChIP-seq data is plotted across the two categories of genes from panel C. E) Differential mRNA-seq expression values (log2fc from DESeq2) is plotted for control high (n=817), wapl high

(n=1268) genes that were further subsetted to be within 40 kb from the jet origin, where the differential cohesin binding is the most pronounced. Other genes (n=15800) were used as control. Mann-Whitney test was used to generate p values. F) The proposed model of cohesin loading and loop extrusion events inferred from the perturbation experiments and literature. Activated enhancers are bound by NIPBL which increase the frequency of cohesin loading at these sites. After loading, cohesin extrudes DNA in an effectively two-sided manner. Note that despite being depicted as a singular ring, the data cannot distinguish how many cohesin complexes are at the base of the loop. Upon acute depletion of SMC-3, the binding of NIPBL is unaffected and residual amount of SMC-1 is found at loading site. The extruded loop is abolished. Upon acute depletion of the negative regulator WAPL-1, cohesin further extrudes DNA in two-sided manner away from the jet origin. The extended extrusion revealed that the clash between incoming and outgoing cohesin molecules can stall extrusion. Together, cohesin processivity at each side can be unequal and may be facilitated by transcription moving in the same direction. Despite the lack of immediate effect on transcription, the extruded loops can encompass multiple cis-regulatory elements.

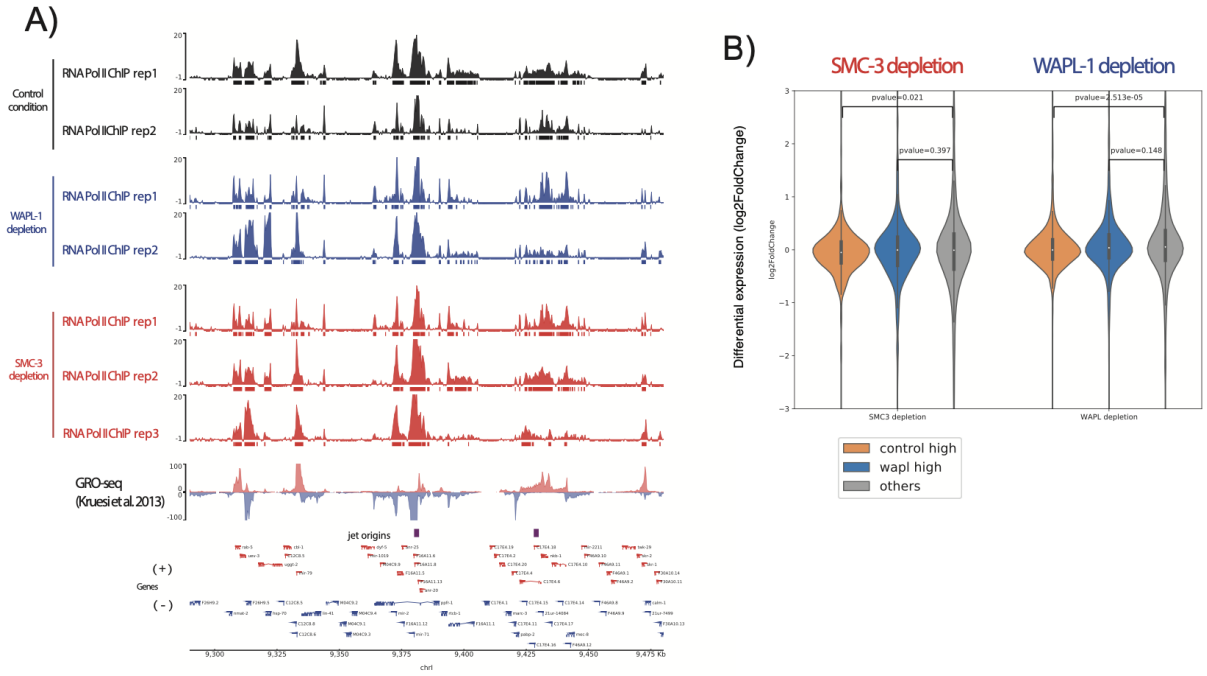

Supplemental Figure 5 Replicates of RNA Pol II and NIPBL ChIP-seq data in control, SMC-3 and WAPL depletion conditions

A) RNA Pol II ChIP-seq tracks for the control, WAPl-1, and SMC-3 depletion conditions at an example region in the region. B) Differential expression values (log2fc from DESeq2) is plotted for three categories of genes upon 4 hr SMC-3 and WAPL-1 depletion (same grouping as done in Figure 8C). No-tag strain was used as control. Mann-Whitney test was used to generate p values.

Discussion

Cohesin and CTCF mediated TAD formation contribute to proper development and normal physiology in the mammalian system, but many organisms, including yeast, worms and plants, contain cohesin but lack CTCF (Heger et al. 2012; Dong et al. 2017). Here, we use *C. elegans* as a model to address the question: what does interphase cohesin do in organisms without CTCF? Our approach was to apply the auxin-inducible degradation system to acutely deplete the cohesin ATPase subunit SMC-3 or its negative regulator WAPL-1 in somatic cells in *C. elegans* larvae. Our results are consistent with a model that preferential loading of cohesin at active enhancers followed by bi-directional loop extrusion forms 3D DNA contact domains that are observed as a Hi-C feature termed chromatin jets (Figure 8F).

Chromatin jets are a conserved feature of 3D genome organization mediated by cohesin

Recent studies including this one demonstrate the existence of jets (aka plumes or fountains) in model species of worms, zebrafish and mammals, suggesting that preferential loading of cohesin followed by bi-directional loop extrusion leads is conserved across species (Liu et al. 2021a; Wike et al. 2021; Guo et al. 2022; Galitsyna et al. 2023; Isiaka et al. 2023). In zebrafish, chromatin jets correlated with enhancer activity across development, and knockdown of pioneer transcription factors eliminated chromatin jets originating at these sites (Galitsyna et al. 2023). In mammalian cells, analysis of cohesin binding upon CTCF site deletion, depletion of pioneer transcription factors, and ectopic recruitment experiments suggest that cohesin is preferentially loaded at enhancers (Dowen et al. 2013; Liu et al. 2021b; Vos et al. 2021; Han et al. 2023). Our work also showed an overlap of jet origins with active enhancers in *C. elegans*, thus preferential loading of cohesin may be a conserved mechanism of regulating 3D DNA contacts surrounding enhancers, even in a compact genome that lacks CTCF.

*NIPBL recruitment to a*ctive *enhancers may facilitate cohesin loading that form chromatin jets*

Based on analysis of individual jets and their genomic context, we observed that the origin of the trajectory of chromatin jets correlates with NIPBL binding. Immunofluorescence analyses of cohesin in the germline showed that *C. elegans* NIPBL (PQN-85/SCC-2) is required for cohesin binding to chromosomes (Ciosk et al. 2000; Seitan et al. 2006; Lightfoot et al. 2011). In many organisms, including *C. elegans*, NIPBL binds to active enhancers (Kranz et al. 2013; Busslinger et al. 2017; Zhu et al. 2021). In yeast, NIPBL interacts with and is recruited by the mediator complex (Mattingly et al. 2022). Therefore, it is possible that transcription factors interaction with the mediator recruits NIPBL to load cohesin at active enhancers.

In mammals, NIPBL is proposed to be a processivity factor that regulates the engagement of cohesin with DNA during loop extrusion (Alonso-Gil and Losada 2023). ChIP-seq analysis of NIPBL upon RNAi depletion of a cohesin subunit in HeLa cells suggested that NIPBL binding at promoters is cohesin dependent (Banigan et al. 2023). In *C. elegans*, we did not observe a change in NIPBL binding upon cohesin or WAPL depletion (Figure 7). Therefore, it is unlikely that NIPBL translocate along with loop extruding cohesin in *C. elegans*. It is possible that the longer processivity of mammalian cohesin compared to that of *C. elegans* is related to NIPBL's processivity function. Differences between NIPBL function in mammals and *C. elegans* may provide insights into the conserved and distinct mechanisms of cohesin regulation in the evolution of small and larger animal genomes.

Chromatin jets and gene regulation

In our study, one hour depletion of cohesin and WAPL resulted in striking changes in the chromatin jets, but not on RNA Pol II binding measured by ChIP-seq and mRNA levels measured by RNA-seq (Figure 8). In the mammalian system, knockdown of cohesin also resulted in subtle changes in gene expression, yet mutations that reduce cohesin dosage or TAD boundaries produce significant changes (Cummings and Rowley 2022; Hafner and Boettiger 2023). It is possible that cohesin acts as a fine-tuner of transcription or function earlier in development, and once an epigenetic state is established, short-term depletion of cohesin does not result in changes in transcription (Pelham-Webb et al. 2020).

A recent preprint presented Hi-C data upon TEV-mediated cleavage of two cohesin kleisin subunits over a period of ~24 hours from L1 larvae to L3 in *C. elegans* (Das et al. 2022). A subsequent preprint called fountains and showed that the cleavage of COH-1 but not SCC-1 eliminated them, supporting the presence of a specialized cohesin for interphase genome organization in *C. elegans* (Isiaka et al. 2023). Authors reported a slight increase in the expression of genes closer to jet origins upon cohesin cleavage. This contrasts with the slight decrease we observed (Figure 8). In both studies RNA-seq was performed in whole animals and the effect was subtle. Thus, further research is required to address potential jet function in gene regulation.

RNA Polymerase II: barrier or facilitator of cohesin loop extrusion?

Earlier studies in yeast suggested that RNA Pol II may push cohesin (Glynn et al. 2004; Lengronne et al. 2004). More recent work used the framework of loop extrusion model and proposed that RNA Pol II and MCM complexes may be barriers to cohesin mediated loop extrusion (Dequeker et al. 2022; Banigan et al. 2023). Our cohesin ChIP-seq data in *C. elegans* produced a pattern consistently observed in many organisms, where distinct peaks of binding are detected at promoters and enhancers (Peters et al. 2008; Rittenhouse and Dowen 2024). We also observe that prominent chromatin jets are formed at regions where cohesin frequently translocate in the same direction as transcription (Figure 7). It is possible that enhancers generally load cohesin, but the transcription increases loading frequency upstream or facilitates cohesin movement, both of which can enhance the observable jet pattern. Alternatively, intermittent stalling by polymerase allows for better capturing of the loops by crosslinking-dependent methods like Hi-C and ChIP-seq.

Clash of loop extruding cohesins creating a barrier effect

Modeling approaches are used to connect the behavior of single cohesin molecules to the population average data produced in Hi-C and we have interpreted our data in light of these studies (Banigan et al. 2020). Our results suggest that frequent loading results in the clash of loop extruding cohesin molecules when these molecules are not removed from the DNA template by WAPL (Figure 5). The resulting structure suggests cohesin continues to loop extrude on one side, while being stalled on the other. Therefore, an asymmetry in the loop extrusion is introduced by a barrier, in this case an incoming cohesin. Supporting our interpretation, computational modeling used the interaction of outgoing and incoming cohesin molecules to

explain the flared structure of fountains in zebrafish (Galitsyna et al. 2023), which are like the chromatin jets in *C. elegans* and unlike the hairpin structures formed by preferential loading and extrusion by bacterial SMCs (Brandao et al. 2021).

Clashing of incoming loop extruders may be a general feature of SMC complexes. In *C. elegans*, a specialized condensin I complex is loaded at distinct cis-regulatory elements on the X chromosomes for dosage compensation (DC) (Kim et al. 2022). The loading sites also act to block loop extrusion by condensin DC (average loop size ~150 kb), thus forming TAD boundaries (Anderson et al. 2019; Rowley et al. 2020). It is possible that frequent loading of condensin DC at one recruitment site block the incoming molecules from another, because condensin loop extrudes in one direction (Kim et al. 2022). In the case of cohesin, the clash of two cohesin molecules stops loop extrusion on the meeting side, but not the other (Figure 5). This supports the idea that unlike condensin, cohesin extrudes DNA in both directions *in vivo*. Intriguingly, we observed that cohesin-mediated loops are shorter on the X chromosome, raising the possibility that condensin reduces cohesin processivity.

Evolution of cohesin activity

The co-evolution of underlying linear genome complexity and cohesin function may explain CTCF being lost in *C. elegans*. In the mammalian system, the relatively large cohesin loops are constrained by positioning of CTCF to prevent ectopic activation of promoters (Levine et al. 2014; Hnisz et al. 2016). *C. elegans* cohesin makes ~10 fold smaller loops compared to the mammalian systems, which seems to scale with gene density (~one gene per 5 versus 100 kb). Our study offers two ideas. First, the shorter processivity of *C. elegans* cohesin may be extrinsic, due to frequent encounters with *in vivo* barriers of loop extrusion, including clashes between cohesin molecules in a compact genome. Second, intrinsic factors may also reduce processivity. For instance, NIPBL may have a more limited role in the processivity of cohesin in *C. elegans* compared to the mammalian system.

Whether cohesin mediated DNA loops reduce *cis*-element search space (Hsieh et al. 2022), or functions to cyclically accumulate factors for promoter activation (Xiao et al. 2021), the relatively weak cohesin of *C. elegans* fits its underlying compact genome, where enhancers are intragenic or immediately upstream of promoter (Reinke et al. 2013). The presence of chromatin jets in *C. elegans* argues that preferential loading of cohesin at active enhancers is a conserved mechanism of 3D genome regulation regardless of genome size and CTCF presence. Within the context of a compact animal genome, how cohesin functions to regulate the 3D contacts of enhancers to accomplish cell-type specific gene expression is an intriguing question for future studies.

Acknowledgements:
JK and SE, and research in this manuscript were supported by NIGMS of the National Institutes of Health under award number R35 GM130311. Jun Kim was partially supported by NIGMS Predoctoral Fellowship T32HD007520. We thank Dominic Balcon for testing cohesin antibodies and Gencore at the NYU Center for Genomics and Systems Biology for sequencing and raw data processing.

Author Contributions:
JK and SE conceptualized the project and designed experiments. JK and HW performed experiments. JK performed data analysis JK and SE prepared figures and wrote the manuscript.

Declaration of interests:
None

References

Abdennur N, Mirny LA. 2020. Cooler: scalable storage for Hi-C data and other genomically labeled arrays. *Bioinformatics* **36**: 311-316.

Albritton SE, Ercan S. 2018. Caenorhabditis elegans Dosage Compensation: Insights into Condensin-Mediated Gene Regulation. *Trends Genet* **34**: 41-53.

Albritton SE, Kranz AL, Rao P, Kramer M, Dieterich C, Ercan S. 2014. Sex-biased gene expression and evolution of the x chromosome in nematodes. *Genetics* **197**: 865-883.

Allen MA, Hillier LW, Waterston RH, Blumenthal T. 2011. A global analysis of C. elegans trans-splicing. *Genome Res* **21**: 255-264.

Alonso-Gil D, Cuadrado A, Gimenez-Llorente D, Rodriguez-Corsino M, Losada A. 2023. Different NIPBL requirements of cohesin-STAG1 and cohesin-STAG2. *Nat Commun* **14**: 1326.

Alonso-Gil D, Losada A. 2023. NIPBL and cohesin: new take on a classic tale. *Trends Cell Biol* **33**: 860-871.

Amemiya HM, Kundaje A, Boyle AP. 2019. The ENCODE Blacklist: Identification of Problematic Regions of the Genome. *Sci Rep* **9**: 9354.

Anders S, Pyl PT, Huber W. 2015. HTSeq--a Python framework to work with high-throughput sequencing data. *Bioinformatics* **31**: 166-169.

Anderson EC, Frankino PA, Higuchi-Sanabria R, Yang Q, Bian Q, Podshivalova K, Shin A, Kenyon C, Dillin A, Meyer BJ. 2019. X Chromosome Domain Architecture Regulates Caenorhabditis elegans Lifespan but Not Dosage Compensation. *Dev Cell* **51**: 192-207 e196.

Arnould C, Rocher V, Finoux AL, Clouaire T, Li K, Zhou F, Caron P, Mangeot PE, Ricci EP, Mourad R et al. 2021. Loop extrusion as a mechanism for formation of DNA damage repair foci. *Nature* **590**: 660-665.

Banigan EJ, Tang W, van den Berg AA, Stocsits RR, Wutz G, Brandao HB, Busslinger GA, Peters JM, Mirny LA. 2023. Transcription shapes 3D chromatin organization by interacting with loop extrusion. *Proc Natl Acad Sci U S A* **120**: e2210480120.

Banigan EJ, van den Berg AA, Brandao HB, Marko JF, Mirny LA. 2020. Chromosome organization by one-sided and two-sided loop extrusion. *Elife* **9**.

Bian Q, Anderson EC, Yang Q, Meyer BJ. 2020. Histone H3K9 methylation promotes formation of genome compartments in Caenorhabditis elegans via chromosome compaction and perinuclear anchoring. *Proc Natl Acad Sci U S A* **117**: 11459-11470.

Brandao HB, Paul P, van den Berg AA, Rudner DZ, Wang X, Mirny LA. 2019. RNA polymerases as moving barriers to condensin loop extrusion. *Proc Natl Acad Sci U S A* **116**: 20489-20499.

Brandao HB, Ren Z, Karaboja X, Mirny LA, Wang X. 2021. DNA-loop-extruding SMC complexes can traverse one another in vivo. *Nat Struct Mol Biol* **28**: 642-651.

Busslinger GA, Stocsits RR, van der Lelij P, Axelsson E, Tedeschi A, Galjart N, Peters JM. 2017. Cohesin is positioned in mammalian genomes by transcription, CTCF and Wapl. *Nature* **544**: 503-507.

Ciosk R, Shirayama M, Shevchenko A, Tanaka T, Toth A, Shevchenko A, Nasmyth K. 2000. Cohesin's binding to chromosomes depends on a separate complex consisting of Scc2 and Scc4 proteins.

Mol Cell **5**: 243-254.
Corsi F, Rusch E, Goloborodko A. 2023. Loop extrusion rules: the next generation. *Curr Opin Genet Dev* **81**: 102061.
Crane E, Bian Q, McCord RP, Lajoie BR, Wheeler BS, Ralston EJ, Uzawa S, Dekker J, Meyer BJ. 2015. Condensin-driven remodelling of X chromosome topology during dosage compensation. *Nature* **523**: 240-244.
Cuadrado A, Losada A. 2020. Specialized functions of cohesins STAG1 and STAG2 in 3D genome architecture. *Curr Opin Genet Dev* **61**: 9-16.
Cummings CT, Rowley MJ. 2022. Implications of Dosage Deficiencies in CTCF and Cohesin on Genome Organization, Gene Expression, and Human Neurodevelopment. *Genes (Basel)* **13**.
da Costa-Nunes JA, Noordermeer D. 2023. TADs: Dynamic structures to create stable regulatory functions. *Curr Opin Struct Biol* **81**: 102622.
Danecek P, Bonfield JK, Liddle J, Marshall J, Ohan V, Pollard MO, Whitwham A, Keane T, McCarthy SA, Davies RM, Li H. 2021. Twelve years of SAMtools and BCFtools. *Gigascience* **10**.
Das M, Semple JI, Volodkina V, Haemmerli A, Scotton J, Gitchev T, Annan A, Statzer C, Ewald CY, Mozziconacci J et al. 2022. Condensin I folds the C. elegans genome. *bioRxiv* doi:10.1101/2022.06.14.495661: 2022.2006.2014.495661.
Daugherty AC, Yeo RW, Buenrostro JD, Greenleaf WJ, Kundaje A, Brunet A. 2017. Chromatin accessibility dynamics reveal novel functional enhancers in C. elegans. *Genome Res* **27**: 2096-2107.
Davidson IF, Barth R, Zaczek M, van der Torre J, Tang W, Nagasaka K, Janissen R, Kerssemakers J, Wutz G, Dekker C, Peters JM. 2023. CTCF is a DNA-tension-dependent barrier to cohesin-mediated loop extrusion. *Nature* **616**: 822-827.
Davidson IF, Bauer B, Goetz D, Tang W, Wutz G, Peters JM. 2019. DNA loop extrusion by human cohesin. *Science* **366**: 1338-1345.
Dequeker BJH, Scherr MJ, Brandao HB, Gassler J, Powell S, Gaspar I, Flyamer IM, Lalic A, Tang W, Stocsits R et al. 2022. MCM complexes are barriers that restrict cohesin-mediated loop extrusion. *Nature* **606**: 197-203.
Dong P, Tu X, Chu PY, Lu P, Zhu N, Grierson D, Du B, Li P, Zhong S. 2017. 3D Chromatin Architecture of Large Plant Genomes Determined by Local A/B Compartments. *Mol Plant* **10**: 1497-1509.
Dowen JM, Bilodeau S, Orlando DA, Hubner MR, Abraham BJ, Spector DL, Young RA. 2013. Multiple structural maintenance of chromosome complexes at transcriptional regulatory elements. *Stem Cell Reports* **1**: 371-378.
Durand NC, Shamim MS, Machol I, Rao SS, Huntley MH, Lander ES, Aiden EL. 2016. Juicer Provides a One-Click System for Analyzing Loop-Resolution Hi-C Experiments. *Cell Syst* **3**: 95-98.
Ercan S, Dick LL, Lieb JD. 2009. The C. elegans dosage compensation complex propagates dynamically and independently of X chromosome sequence. *Curr Biol* **19**: 1777-1787.
Evans KJ, Huang N, Stempor P, Chesney MA, Down TA, Ahringer J. 2016. Stable Caenorhabditis elegans chromatin domains separate broadly expressed and developmentally regulated genes. *Proc Natl Acad Sci U S A* **113**: E7020-E7029.
Fudenberg G, Abdennur N, Imakaev M, Goloborodko A, Mirny LA. 2017. Emerging Evidence of Chromosome Folding by Loop Extrusion. *Cold Spring Harb Symp Quant Biol* **82**: 45-55.
Galitsyna A, Ulianov SV, Bykov NS, Veil M, Gao M, Perevoschikova K, Gelfand M, Razin SV, Mirny L, Onichtchouk D. 2023. Extrusion fountains are hallmarks of chromosome organization emerging upon zygotic genome activation. *bioRxiv* doi:10.1101/2023.07.15.549120.
Gandhi R, Gillespie PJ, Hirano T. 2006. Human Wapl is a cohesin-binding protein that promotes sister-chromatid resolution in mitotic prophase. *Curr Biol* **16**: 2406-2417.
Gassler J, Brandao HB, Imakaev M, Flyamer IM, Ladstatter S, Bickmore WA, Peters JM, Mirny LA, Tachibana K. 2017. A mechanism of cohesin-dependent loop extrusion organizes zygotic genome architecture. *EMBO J* **36**: 3600-3618.
Girard LR, Fiedler TJ, Harris TW, Carvalho F, Antoshechkin I, Han M, Sternberg PW, Stein LD, Chalfie

M. 2007. WormBook: the online review of Caenorhabditis elegans biology. *Nucleic Acids Res* **35**: D472-475.
Glynn EF, Megee PC, Yu HG, Mistrot C, Unal E, Koshland DE, DeRisi JL, Gerton JL. 2004. Genome-wide mapping of the cohesin complex in the yeast Saccharomyces cerevisiae. *PLoS Biol* **2**: E259.
Graham TG, Wang X, Song D, Etson CM, van Oijen AM, Rudner DZ, Loparo JJ. 2014. ParB spreading requires DNA bridging. *Genes Dev* **28**: 1228-1238.
Guo Y, Al-Jibury E, Garcia-Millan R, Ntagiantas K, King JWD, Nash AJ, Galjart N, Lenhard B, Rueckert D, Fisher AG et al. 2022. Chromatin jets define the properties of cohesin-driven in vivo loop extrusion. *Mol Cell* **82**: 3769-3780 e3765.
Hafner A, Boettiger A. 2023. The spatial organization of transcriptional control. *Nat Rev Genet* **24**: 53-68.
Han R, Huang Y, Vaandrager I, Allahyar A, Magnitov M, Verstegen MJAM, Wit Ed, Krijger PHL, Laat Wd. 2023. Targeted cohesin loading characterizes the entry and exit sites of loop extrusion trajectories. *bioRxiv* doi:10.1101/2023.01.04.522689: 2023.2001.2004.522689.
Hassler M, Shaltiel IA, Haering CH. 2018. Towards a Unified Model of SMC Complex Function. *Curr Biol* **28**: R1266-R1281.
Heger P, Marin B, Bartkuhn M, Schierenberg E, Wiehe T. 2012. The chromatin insulator CTCF and the emergence of metazoan diversity. *Proc Natl Acad Sci U S A* **109**: 17507-17512.
Heger P, Marin B, Schierenberg E. 2009. Loss of the insulator protein CTCF during nematode evolution. *BMC Mol Biol* **10**: 84.
Hernandez MR, Davis MB, Jiang J, Brouhard EA, Severson AF, Csankovszki G. 2018. Condensin I protects meiotic cohesin from WAPL-1 mediated removal. *PLoS Genet* **14**: e1007382.
Hnisz D, Day DS, Young RA. 2016. Insulated Neighborhoods: Structural and Functional Units of Mammalian Gene Control. *Cell* **167**: 1188-1200.
Ho JW, Jung YL, Liu T, Alver BH, Lee S, Ikegami K, Sohn KA, Minoda A, Tolstorukov MY, Appert A et al. 2014. Comparative analysis of metazoan chromatin organization. *Nature* **512**: 449-452.
Hopfner KP, Tainer JA. 2003. Rad50/SMC proteins and ABC transporters: unifying concepts from high-resolution structures. *Curr Opin Struct Biol* **13**: 249-255.
Hsieh TS, Cattoglio C, Slobodyanyuk E, Hansen AS, Darzacq X, Tjian R. 2022. Enhancer-promoter interactions and transcription are largely maintained upon acute loss of CTCF, cohesin, WAPL or YY1. *Nat Genet* **54**: 1919-1932.
Ishiguro KI. 2019. The cohesin complex in mammalian meiosis. *Genes Cells* **24**: 6-30.
Isiaka BN, Semple JI, Haemmerli A, Thapliyal S, Stojanovski K, Das M, Gilbert N, Glauser DA, Towbin B, Jost D, Meister P. 2023. Cohesin forms fountains at active enhancers in C. elegans. *bioRxiv* doi:10.1101/2023.07.14.549011: 2023.2007.2014.549011.
Kagey MH, Newman JJ, Bilodeau S, Zhan Y, Orlando DA, van Berkum NL, Ebmeier CC, Goossens J, Rahl PB, Levine SS et al. 2010. Mediator and cohesin connect gene expression and chromatin architecture. *Nature* **467**: 430-435.
Kim D, Langmead B, Salzberg SL. 2015. HISAT: a fast spliced aligner with low memory requirements. *Nat Methods* **12**: 357-360.
Kim J, Jimenez DS, Ragipani B, Zhang B, Street LA, Kramer M, Albritton SE, Winterkorn LH, Morao AK, Ercan S. 2022. Condensin DC loads and spreads from recruitment sites to create loop-anchored TADs in C. elegans. *Elife* **11**.
Kim Y, Shi Z, Zhang H, Finkelstein IJ, Yu H. 2019. Human cohesin compacts DNA by loop extrusion. *Science* **366**: 1345-1349.
Kranz AL, Jiao CY, Winterkorn LH, Albritton SE, Kramer M, Ercan S. 2013. Genome-wide analysis of condensin binding in Caenorhabditis elegans. *Genome Biol* **14**: R112.
Kruesi WS, Core LJ, Waters CT, Lis JT, Meyer BJ. 2013. Condensin controls recruitment of RNA polymerase II to achieve nematode X-chromosome dosage compensation. *Elife* **2**: e00808.
Kueng S, Hegemann B, Peters BH, Lipp JJ, Schleiffer A, Mechtler K, Peters JM. 2006. Wapl controls the dynamic association of cohesin with chromatin. *Cell* **127**: 955-967.
Langmead B, Salzberg SL. 2012. Fast gapped-read alignment with Bowtie 2. *Nat Methods* **9**: 357-359.

Lengronne A, Katou Y, Mori S, Yokobayashi S, Kelly GP, Itoh T, Watanabe Y, Shirahige K, Uhlmann F. 2004. Cohesin relocation from sites of chromosomal loading to places of convergent transcription. *Nature* **430**: 573-578.

Levine M, Cattoglio C, Tjian R. 2014. Looping back to leap forward: transcription enters a new era. *Cell* **157**: 13-25.

Lightfoot J, Testori S, Barroso C, Martinez-Perez E. 2011. Loading of meiotic cohesin by SCC-2 is required for early processing of DSBs and for the DNA damage checkpoint. *Curr Biol* **21**: 1421-1430.

Liu NQ, Magnitov M, Schijns M, Schaik Tv, Weide RHvd, Teunissen H, Steensel Bv, Wit Ed. 2021a. Rapid depletion of CTCF and cohesin proteins reveals dynamic features of chromosome architecture. *bioRxiv* doi:10.1101/2021.08.27.457977: 2021.2008.2027.457977.

Liu NQ, Maresca M, van den Brand T, Braccioli L, Schijns M, Teunissen H, Bruneau BG, Nora EP, de Wit E. 2021b. WAPL maintains a cohesin loading cycle to preserve cell-type-specific distal gene regulation. *Nat Genet* **53**: 100-109.

Liu T, Rechtsteiner A, Egelhofer TA, Vielle A, Latorre I, Cheung MS, Ercan S, Ikegami K, Jensen M, Kolasinska-Zwierz P et al. 2011. Broad chromosomal domains of histone modification patterns in C. elegans. *Genome Res* **21**: 227-236.

Love MI, Huber W, Anders S. 2014. Moderated estimation of fold change and dispersion for RNA-seq data with DESeq2. *Genome Biol* **15**: 550.

Mattingly M, Seidel C, Munoz S, Hao Y, Zhang Y, Wen Z, Florens L, Uhlmann F, Gerton JL. 2022. Mediator recruits the cohesin loader Scc2 to RNA Pol II-transcribed genes and promotes sister chromatid cohesion. *Curr Biol* **32**: 2884-2896 e2886.

Mito Y, Sugimoto A, Yamamoto M. 2003. Distinct developmental function of two Caenorhabditis elegans homologs of the cohesin subunit Scc1/Rad21. *Mol Biol Cell* **14**: 2399-2409.

Morao AK, Kim J, Obaji D, Sun S, Ercan S. 2022. Topoisomerases I and II facilitate condensin DC translocation to organize and repress X chromosomes in C. elegans. *Mol Cell* **82**: 4202-4217 e4205.

Muir KW, Li Y, Weis F, Panne D. 2020. The structure of the cohesin ATPase elucidates the mechanism of SMC-kleisin ring opening. *Nat Struct Mol Biol* **27**: 233-239.

Nelson CE, Hersh BM, Carroll SB. 2004. The regulatory content of intergenic DNA shapes genome architecture. *Genome Biol* **5**: R25.

Pelham-Webb B, Murphy D, Apostolou E. 2020. Dynamic 3D Chromatin Reorganization during Establishment and Maintenance of Pluripotency. *Stem Cell Reports* **15**: 1176-1195.

Peters JM, Tedeschi A, Schmitz J. 2008. The cohesin complex and its roles in chromosome biology. *Genes Dev* **22**: 3089-3114.

Polovnikov KE, Slavov B, Belan S, Imakaev M, Brandão HB, Mirny LA. 2023. Fractal polymer with loops recapitulates key features of chromosome organization. *bioRxiv* doi:10.1101/2022.02.01.478588: 2022.2002.2001.478588.

Ramirez F, Bhardwaj V, Arrigoni L, Lam KC, Gruning BA, Villaveces J, Habermann B, Akhtar A, Manke T. 2018. High-resolution TADs reveal DNA sequences underlying genome organization in flies. *Nat Commun* **9**: 189.

Ramirez-Gonzalez RH, Bonnal R, Caccamo M, Maclean D. 2012. Bio-samtools: Ruby bindings for SAMtools, a library for accessing BAM files containing high-throughput sequence alignments. *Source Code Biol Med* **7**: 6.

Reinke V, Krause M, Okkema P. 2013. Transcriptional regulation of gene expression in C. elegans. *WormBook* doi:10.1895/wormbook.1.45.2: 1-34.

Rittenhouse NL, Dowen JM. 2024. Cohesin regulation and roles in chromosome structure and function. *Curr Opin Genet Dev* **85**: 102159.

Roberts A, Pimentel H, Trapnell C, Pachter L. 2011. Identification of novel transcripts in annotated genomes using RNA-Seq. *Bioinformatics* **27**: 2325-2329.

Rowley MJ, Poulet A, Nichols MH, Bixler BJ, Sanborn AL, Brouhard EA, Hermetz K, Linsenbaum H,

Csankovszki G, Lieberman Aiden E, Corces VG. 2020. Analysis of Hi-C data using SIP effectively identifies loops in organisms from C. elegans to mammals. *Genome Res* **30**: 447-458.
Sawh AN, Mango SE. 2022. Chromosome organization in 4D: insights from C. elegans development. *Curr Opin Genet Dev* **75**: 101939.
Seitan VC, Banks P, Laval S, Majid NA, Dorsett D, Rana A, Smith J, Bateman A, Krpic S, Hostert A et al. 2006. Metazoan Scc4 homologs link sister chromatid cohesion to cell and axon migration guidance. *PLoS Biol* **4**: e242.
Severson AF, Ling L, van Zuylen V, Meyer BJ. 2009. The axial element protein HTP-3 promotes cohesin loading and meiotic axis assembly in C. elegans to implement the meiotic program of chromosome segregation. *Genes Dev* **23**: 1763-1778.
Severson AF, Meyer BJ. 2014. Divergent kleisin subunits of cohesin specify mechanisms to tether and release meiotic chromosomes. *Elife* **3**: e03467.
Shi B, Guo X, Wu T, Sheng S, Wang J, Skogerbo G, Zhu X, Chen R. 2009. Genome-scale identification of Caenorhabditis elegans regulatory elements by tiling-array mapping of DNase I hypersensitive sites. *BMC Genomics* **10**: 92.
Sullivan NL, Marquis KA, Rudner DZ. 2009. Recruitment of SMC by ParB-parS organizes the origin region and promotes efficient chromosome segregation. *Cell* **137**: 697-707.
Sulston JE, Horvitz HR. 1977. Post-embryonic cell lineages of the nematode, Caenorhabditis elegans. *Dev Biol* **56**: 110-156.
Vos ESM, Valdes-Quezada C, Huang Y, Allahyar A, Verstegen M, Felder AK, van der Vegt F, Uijttewaal ECH, Krijger PHL, de Laat W. 2021. Interplay between CTCF boundaries and a super enhancer controls cohesin extrusion trajectories and gene expression. *Mol Cell* **81**: 3082-3095 e3086.
Wang X, Brandao HB, Le TB, Laub MT, Rudner DZ. 2017. Bacillus subtilis SMC complexes juxtapose chromosome arms as they travel from origin to terminus. *Science* **355**: 524-527.
Wang X, Hughes AC, Brandao HB, Walker B, Lierz C, Cochran JC, Oakley MG, Kruse AC, Rudner DZ. 2018. In Vivo Evidence for ATPase-Dependent DNA Translocation by the Bacillus subtilis SMC Condensin Complex. *Mol Cell* **71**: 841-847 e845.
Wike CL, Guo Y, Tan M, Nakamura R, Shaw DK, Diaz N, Whittaker-Tademy AF, Durand NC, Aiden EL, Vaquerizas JM et al. 2021. Chromatin architecture transitions from zebrafish sperm through early embryogenesis. *Genome Res* **31**: 981-994.
Wolff J, Bhardwaj V, Nothjunge S, Richard G, Renschler G, Gilsbach R, Manke T, Backofen R, Ramirez F, Gruning BA. 2018. Galaxy HiCExplorer: a web server for reproducible Hi-C data analysis, quality control and visualization. *Nucleic Acids Res* **46**: W11-W16.
Wood AJ, Severson AF, Meyer BJ. 2010. Condensin and cohesin complexity: the expanding repertoire of functions. *Nat Rev Genet* **11**: 391-404.
Xiao JY, Hafner A, Boettiger AN. 2021. How subtle changes in 3D structure can create large changes in transcription. *Elife* **10**.
Yoshimura J, Ichikawa K, Shoura MJ, Artiles KL, Gabdank I, Wahba L, Smith CL, Edgley ML, Rougvie AE, Fire AZ et al. 2019. Recompleting the Caenorhabditis elegans genome. *Genome Res* **29**: 1009-1022.
Yu Z, Kim HJ, Dernburg AF. 2023. ATM signaling modulates cohesin behavior in meiotic prophase and proliferating cells. *Nat Struct Mol Biol* **30**: 436-450.
Zhang L, Ward JD, Cheng Z, Dernburg AF. 2015. The auxin-inducible degradation (AID) system enables versatile conditional protein depletion in C. elegans. *Development* **142**: 4374-4384.
Zhu Y, Denholtz M, Lu H, Murre C. 2021. Calcium signaling instructs NIPBL recruitment at active enhancers and promoters via distinct mechanisms to reconstruct genome compartmentalization. *Genes Dev* **35**: 65-81.